LBNL-45246

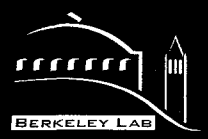

ERNEST ORLANDO LAWRENCE
BERKELEY NATIONAL LABORATORY

The Ideal Strength and Mechanical Hardness of Solids

Christopher R. Krenn

Materials Sciences Division

April 2000

Ph.D. Thesis

LBNL-45246

The Ideal Strength and Mechanical Hardness of Solids

Christopher Robert Krenn
Ph.D. Thesis

Department of Materials Science and Mineral Engineering
University of California, Berkeley

and

Center for Advanced Materials
Materials Sciences Division
Ernest Orlando Lawrence Berkeley National Laboratory
University of California
Berkeley, CA 94720

April 2000

This work was supported by the Director, Office of Science, Office of Basic Energy Sciences, Materials Sciences Division, of the U.S. Department of Energy under Contract No. DE-AC03-76SF00098.

The Ideal Strength and Mechanical Hardness of Solids

by

Christopher Robert Krenn

Abstract

The Ideal Strength and Mechanical Hardness of Solids

by

Christopher Robert Krenn
Doctor of Philosophy in Materials Science and Mineral Engineering

University of California at Berkeley

Professor J. W. Morris Jr., Chair

Relationships between intrinsic mechanical hardness and atomic-scale properties are reviewed. Hardness scales closely and linearly with shear modulus for a given class of material (covalent, ionic or metallic). A two-parameter fit and a Peierls-stress model produce a more universal scaling relationship, but no model can explain differences in hardness between the transition metal carbides and nitrides. Calculations of "ideal strength" (defined by the limit of elastic stability of a perfect crystal) are proposed.

The ideal shear strengths of fcc aluminum and copper are calculated using *ab initio* techniques and allowing for structural relaxation of all five strain components other than the imposed strain. The strengths of Al and Cu are similar (8–9% of the shear modulus), but the geometry of the relaxations in Al and Cu is very different. The relaxations are consistent with experimentally measured third-order elastic constants.

The general thermodynamic conditions of elastic stability that set the upper limits of mechanical strength are derived. The conditions of stability are shown for cubic (hydrostatic), tetragonal (tensile) and monoclinic (shear) distortions of a cubic crystal. The implications of this stability analysis to first-principles calculations of ideal strength are discussed, and a method to detect instabilities orthogonal to the direction of the applied stress is identified.

The relaxed ideal shear and tensile strengths of bcc tungsten are also calculated using *ab initio* techniques and are favorably compared to recent nanoindentation measurements. The {100} tensile strength (29.5 GPa) is governed by the Bain instability. The shear strengths in the weak directions on {110}, {112}, and {123} planes are very nearly equal ($\approx$ 18 GPa) and occur at approximately the same strain (17–18%). This isotropy is a function of the linear elastic isotropy for shear in directions containing $\langle 111 \rangle$ in bcc and of the atomic configurations of energetic saddle points reached during shear. This isotropy may also explain the prevalence of the pencil glide of dislocations in bcc metals.

A final chapter presents some recent ideal strength calculations of TiC and TiN and discusses future directions for research.

Keywords: mechanical hardness, Peierls stress, ideal strength, elastic stability, pencil glide.

To my wife, Lilly, and my mother, Mary,
and in memory of my father, Joseph.

Contents

List of Figures

List of Tables

Acknowledgments

The research presented in this dissertation was done in the course of an ongoing collaborative project that began in 1996. Much of the material has previously been published or submitted for publication as journal articles or conference proceedings that were coauthored with Marvin L. Cohen, Jisoon Ihm, Seung-Hoon Jhi, J. W. Morris Jr. and David Roundy. I gratefully acknowledge their permission to reproduce some of this coauthored work in this dissertation.

David Roundy did all of the *ab initio* total-energy calculations that are presented in Chapters 2 and 4. Michel Côté provided valuable advice in computational methods. Computational resources have been provided by the National Science Foundation at the National Center for Supercomputing Applications and by the National Energy Research Scientific Computing Center, which is supported by the Office of Energy Research of the U. S. Department of Energy under Contract No. DE-AC03-76SF00098.

J. W. Morris Jr. completed the original thermodynamic analysis that is described in Section 3.2. Communications with S. Yip and Ju Li about Chapter 3 are also appreciated.

During my studies, I was financially supported as a graduate student research assistant by the Director, Office of Energy Research, Office of Basic Energy Sciences, Materials Sciences Division of the U. S. Department of Energy, and by the Laboratory Directed Research and Development Program of Lawrence Berkeley National Laboratory under the U. S. Department of Energy. All Department of Energy support was under Contract No. DE-AC03-76SF00098.

I deeply appreciate the continued confidence and freedom that my advisor, J. W. Morris, Jr. has entrusted me with in my graduate career. I enjoyed the challenging questions posed by my qualifying exam committee: R. O. Ritchie (chair), D. C. Chrzan, D. R. Olander and T. Sands. I am grateful for the helpful criticism and advice offered by my dissertation committee: J. W. Morris, Jr., M. L. Cohen and D. C. Chrzan. David Roundy has been a wonderful scientific partner and collaborator.

I am thankful for the support provided by all of the members of the Morris Group past and present. Jane Fortado and Jackie Gamble helped me through the thickets of LBNL's administration and with graphic design. Pete Skarpelos and Koji Sato gave me a lot of help in my qualifying exam preparation. Dave Mitlin helped me understand point groups and crystallography. Jin Chan kept reminding me of the importance of experimental measurements. It has been a

great pleasure to learn and work with Andy, Carlos, Carol, Chris Keller, Dave Clatterbuck, Heidi, Ho Geon, Monica, Pamela, Seung-Hyuk, Tae-Kyu and Zhen.

As always, I am grateful to my mother for allowing me to follow my dreams and to my wife, Lilly, for sharing them with me.

Chapter 1

Atomic Bonding and Mechanical Hardness[†]

1.1 Introduction

For many years, scientists have tried to understand what makes a material inherently strong or hard from an atomic perspective. For the purposes of this dissertation, I will be concerned with the inherent hardness of a material, which I will define as the hardness of a perfect crystal, and I will ignore the many beneficial effects of impurity atoms, second phase particles, work hardening, and other microstructural modifications. Recent theoretical studies of superhard materials have focused on the optimization of bulk modulus and have suggested, for example, that as the calculated bulk modulus of some carbon nitride structures can approach [2] or exceed [3] that of diamond, the mechanical hardnesses of these structures could exceed that of diamond as well. However, the connection between what makes a material stiff (having large elastic moduli) and hard (possessing great resistance to permanent deformation) is still not completely understood.

A number of scaling relationships have been proposed for macroscopic hardness as a function of atomistically defined crystal properties. Hardness, which is typically measured by indentation techniques, has been found to be an increasing function of volumetric lattice energy [4], bulk modulus [5], shear modulus [6, 7], and the size of the electronic band gap [8]. Each of these relationships works well for a certain set of materials, but none are universal. In particular, the hardness of metals is always observed to be much less than ionically or covalently bonded solids at a given value of elastic stiffness or volumetric lattice energy. Figure 1.1 shows a plot of indentation hardness versus elastic shear modulus for a wide variety of materials examined in this research. The slope of all of the trend lines is unity, indicating a linear relationship, and it is clear that covalent solids are harder than metals at a given shear stiffness.

[†]Some of the material in this chapter has been published in Ref. [1].

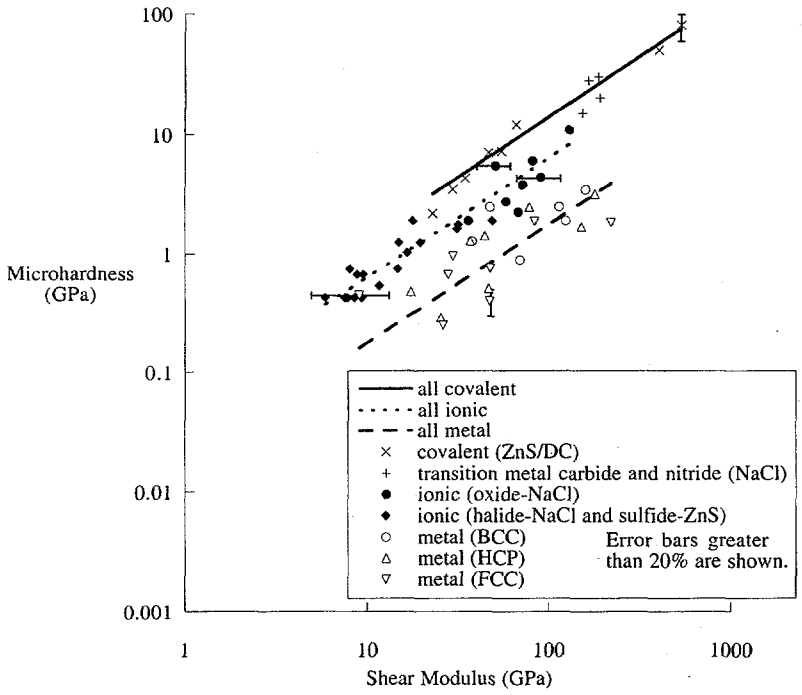

Figure 1.1: Log-log plot of bulk hardness as a function of shear modulus for 3 different classes of materials (covalent, ionic and metallic) with the diamond cubic (dc), body centered cubic (bcc), hexagonal close packed (hcp), face centered cubic (fcc), NaCl, and ZnS structures.

1.2 Universal Scaling Relationships for Hardness

The functional dependence of hardness on elastic constants and lattice energies is justified because hardness is a measure of the resistance of a material to permanent plastic deformation. The mechanism for this deformation in almost all crystalline materials, including diamond [9], involves the movement of dislocations, and so hardness will scale with the resistance to dislocation motion. Lattice energies offer a measure of the strength of atomic bonds. Since the movement of a dislocation even by kink mechanisms requires the complete breaking of a bond, dimensional analysis suggests that the stress (force/length^2) required to break this bond be proportional to the volumetric lattice energy (force $\times$ length/length^3). The scaling of hardness with elastic properties can be justified as follows. To move a dislocation sitting in a minimum of a periodic energy field, enough stress must be applied to overcome an elastic energy barrier. For a given type of bonding the barrier height will be proportional to the curvature of the energy well which is directly proportional to the elastic shear modulus. Since the shear modulus is in general proportional to the bulk modulus, the hardness and Peierls stress will then be proportional to the bulk modulus as well. However, since the proportionality is indirect, one would not expect the scaling to be universal. In particular, the shape of the energy well will be a function of the type of bonding. For more directional bonding, the barrier and thus the hardness will be larger for a given shear modulus. Figure 1.1 and Tables 1.1–1.3 show that the hardnesses of covalently and ionically bonded materials are significantly larger than the hardnesses of metals of equivalent stiffness.

The data used for in Figure 1.1 is shown in Tables 1.1–1.3 and were compiled from a variety of sources. Structures come from Wyckoff [11], and unless otherwise noted, single crystal elastic constants are taken from the Landolt-Börstein handbook, series III, volume 29a [10]. Microhardnesses of ionic materials were estimated from Mohs hardness values listed in Plendl and Gielisse [4] using a parabolic curve fit by Beckmann [20] as described by Goble and Scott [5]. Most other hardnesses were tabulated by Ivan'ko [12] and Holleck [13]. Average polycrystalline elastic properties are calculated following Simmons and Wang [21] using an average of the Hashin and Shtrikman upper and lower bounds for cubic materials [22, 23]. The data tabulated and plotted represent two or more complete sets of single crystal elastic constants, except for the data for CN, BN and ZrN. The CN data comes from a series of measurements at varying nitrogen content [14]. The BN data was included because of its technological significance. The ZrN data was included for comparison with ZrC. The hardnesses of the metals also represent two or more room-temperature microhardness measurements. Since none of our modeling takes into account thermal effects, metals with a melting point less than 25°C were excluded (K, Na and Pb).

Empirically, we see that hardness H_v is directly proportional to the shear modulus G, but that the constant of proportionality, A_i, varies with the type

Table 1.1: Crystal structures, nearest-neighbor distances b in Å, elastic constants c_{ij}, elastic shear (G) and bulk (K) moduli, estimated Peierls stresses τ_p and microhardnesses of "covalently" bonded materials. All elastic constants in GPa.

Material[a]	Structure[b]	b[c]	c_{11}	c_{44}	c_{12}	G	K	τ_p	H_v[d]
InSb	ZnS	2.81	66	30	36	23	46	1.8	2.2
InAs	ZnS	2.61	84	40	46	30	59	2.4	3.5
GaSb	ZnS	2.65	88	43	40	34	56	2.9	4.3
GaAs	ZnS	2.45	120	59	54	47	75	3.9	7.0
Ge	dc	2.45	130	67	48	55	75	4.9	7.2
$C_{0.8}N_{0.2}$[e]	amorph.	–	–	–	–	45	65	–	8.4
Si	dc	2.35	170	79	63	66	97	5.8	12
ZrN[15]	NaCl	2.31	–	–	–	150	270	6.0	15
$C_{0.9}N_{0.1}$[d]	amorph.	–	–	–	–	74	110	–	16
TiN[16, 17]	NaCl	2.12	630	170	170	190	320	7.5	20
ZrC	NaCl	2.34	440	150	60	170	190	7.6	28
TiC	NaCl	2.16	510	180	110	190	240	8.2	30
BN[f]	ZnS	1.57	820	480	190	410	400	39	50
C(d)	dc	1.54	1100	580	120	530	440	54	80

[a] References refer to source of elastic constants if not from Landolt-Börstein LBIII/29a [10].

[b] dc: diamond cubic.

[c] nearest-neighbor distances are derived from the lattice constants tabulated by Wyckoff [11].

[d] Hardnesses in general are from Ivank'ko and Holleck [12, 13]. Hardnesses of CN films are from Yang [14]. Hardness of diamond is from Field [9].

[e] Young's moduli are from Yang [14]. Shear and bulk moduli are calculated assuming Poisson's ratio $\nu = 0.22$. This value was determined by interpolation from a tabulation of the Young's moduli and Poisson's ratio of other dc and ZnS structure materials.

[f] Single crystal elastic constants are from Grimsditch et al. [18] and yield a bulk modulus of 400 ± 20 GPa. However, measurements (369 ± 14 GPa) and calculations (363–370 GPa) of bulk modulus by Knittle et al. [19] suggest that the results of Grimsditch et al. may be systematically high.

Table 1.2: Crystal structures, nearest-neighbor distances b in Å, elastic constants c_{ij}, elastic shear (G) and bulk (K) moduli, estimated Peierls stresses τ_p and microhardnesses of "ionically" bonded materials. All elastic constants in GPa.

Material[a]	Structure	b[b]	c_{11}	c_{44}	c_{12}	G	K	τ_p	H_v[c]
KI	NaCl	3.53	27	3.7	4.3	5.9	12	0.21	0.43
RbCl	NaCl	3.29	36	4.7	6.3	7.6	16	0.27	0.43
KBr	NaCl	3.30	35	5.1	5.5	7.8	15	0.29	0.43
NaI	NaCl	3.24	30	7.4	9.0	8.5	16	0.32	0.43
KCl	NaCl	3.15	41	6.3	6.9	9.3	18	0.35	0.43
NaBr	NaCl	2.99	40	10	11	12	20	0.45	0.54
AgBr	NaCl	2.89	56	7.3	33	8.8	41	0.24	0.67
CuBr	ZnS	2.46	45	15	35	9.5	38	0.65	0.67
AgCl	NaCl	2.77	60	6.2	36	8.1	44	0.21	0.75
NaCl	NaCl	2.82	49	13	13	15	25	0.58	0.75
KF	NaCl	2.67	65	13	15	17	32	0.62	1.0
LiBr	NaCl	2.75	39	19	19	15	26	0.58	1.3
LiCl	NaCl	2.56	49	25	22	19	31	0.78	1.3
NaF	NaCl	2.31	97	28	24	31	48	1.3	1.6
ZnS	ZnS	2.34	100	45	65	32	77	2.4	1.8
CdS	ZnS	2.52	77	24	54	18	62	1.2	1.9
BaO	NaCl	2.76	120	34	45	36	71	1.3	1.9
LiF	NaCl	2.01	110	64	46	49	68	2.1	1.9
MnO	NaCl	2.22	230	78	120	68	150	2.4	2.3
SrO	NaCl	2.58	170	56	46	58	87	2.4	2.8
CoO	NaCl	2.13	260	82	150	71	180	2.4	3.8
NiO	NaCl	2.08	250	110	110	90	160	3.5	4.4
NiO	NaCl	2.08	250	110	110	90	160	3.5	4.4
FeO	NaCl	2.15	220	52	120	51	160	1.6	5.5
CaO	NaCl	2.41	220	81	60	81	110	3.4	6.0
MgO	NaCl	2.11	290	160	93	130	160	5.8	11

[a]Elastic constants are from Landolt-Börstein LBIII/29a [10].

[b]Nearest neighbor distances are derived from the lattice constants tabulated by Wyckoff [11].

[c]Microhardnesses estimated from Mohs hardness values (see text for details).

Table 1.3: Crystal structures, nearest-neighbor distances b in Å, elastic shear (G) and bulk (K) moduli, estimated Peierls stresses τ_p and microhardnesses of bcc, fcc and hcp metals. All elastic constants in GPa.

Material[a]	Structure[b]	b[c]	ν	G	K	τ_p	H_v[d]
Al	fcc	2.86	0.35	26	77	0.0078	0.25
Cd	hcp	2.98	0.31	25	58	0.29	0.29
Pd	fcc	2.75	0.38	47	190	0.0099	0.40
Th	fcc	3.60	0.30	9.0	20	0.0040	0.45
Mg	hcp	3.20	0.29	17	35	0.21	0.48
Zn	hcp	2.79	0.24	47	73	0.68	0.51
Au	fcc	2.88	0.42	28	170	0.0038	0.67
Cu	fcc	2.56	0.34	48	140	0.015	0.76
Ta	bcc	2.86	0.34	69	190	0.43	0.89
Ag	fcc	2.89	0.37	29	100	0.0073	0.96
Nb	bcc	2.86	0.40	38	170	0.17	1.3
Zr	hcp	3.21	0.33	37	97	0.38	1.3
Ti	hcp	2.90	0.32	44	110	0.49	1.4
Be	hcp	2.23	0.03	150	110	3.5	1.7
Ir	fcc	2.71	0.25	220	360	0.15	1.9
Ni	fcc	2.49	0.30	84	180	0.037	1.9
Mo	bcc	2.73	0.30	120	260	0.93	1.9
Co	hcp	2.50	0.32	78	190	0.87	2.5
V	bcc	2.62	0.36	48	160	0.26	2.5
Cr	bcc	2.50	0.21	110	160	1.2	2.5
Re	hcp	2.74	0.29	180	370	2.2	3.2
W	bcc	2.74	0.28	160	310	1.3	3.5

[a]Elastic constants are from Landolt-Börstein LBIII/29a [10].

[b]bcc: body centered cubic, fcc: face centered cubic, and hcp: hexagonal close packed.

[c]Nearest neighbor distances are derived from the lattice constants tabulated by Wyckoff [11].

[d]Hardnesses are from Ivan'ko [12].

of bonding in the solid:

$$H_v = A_i G. \tag{1.1}$$

To capture the exponential dependence, we can define a new relationship for A_i:

$$A_i = A_0 \exp(-C_i), \tag{1.2}$$

so that

$$H_v = A_0 G \exp(-C_i), \tag{1.3}$$

where C_i is a function of the bonding type. For the following fitted values of C_i,

$$H_v = \frac{G}{2}\exp(-1),\ H_v = \frac{G}{2}\exp(-2), \text{ and } H_v = \frac{G}{2}\exp(-3), \tag{1.4}$$

Fig. 1.2 shows that the majority of the data can be collapsed onto a single trend line which spans from the softest metals and salts to diamond. In addition, a set of hardness values from thin film specimens of nitrogenated amorphous carbon lie close to the trend line as well.

A more analytical approach to the differences between classes of materials involves estimates of the Peierls stress. The term "Peierls stress" not only refers to the general notion of the stress required to move a dislocation a single Burgers vector, but to a family of mathematical models of this stress first described by Peierls and Nabarro [24, 25]. Essentially, these models offer a modification of the continuum solutions for the stresses and strains around a dislocation by incorporating an elastic shear stress restoring term along the slip plane which is periodic in the Burgers vector. If this stress is assumed to be sinusoidal, an analytic solution is possible which predicts finite strains at the dislocation core and a Peierls stress of the approximate form:

$$\tau_p = \frac{2\,G}{(1-\nu)} \exp\left(\frac{-2\,\pi h}{b(1-\nu)}\right), \tag{1.5}$$

where G is the shear modulus, ν is Poisson's ratio, h is the spacing between slip planes, and b is the Burgers vector. In a recent review of the history of these models of the Peierls stress, Nabarro [26], pointed out some errors in the original derivations and cited Huntington [27] as the accurate solution to the problem as originally posed (the constants result from two Taylor series numerical approximations in the derivation):

$$\tau_p = \frac{\left(0.15 + 0.03\,(b/\eta h)\right)G}{1-\nu} \exp\left(-\frac{2\,\pi\eta h}{b}\right); \qquad \eta = \frac{1}{2(1-\nu)}. \tag{1.6}$$

Figure 1.3 shows hardness plotted as a function of the Huntington Peierls stress. Table 1.4 lists the values of h and b used in the calculations. Except for the

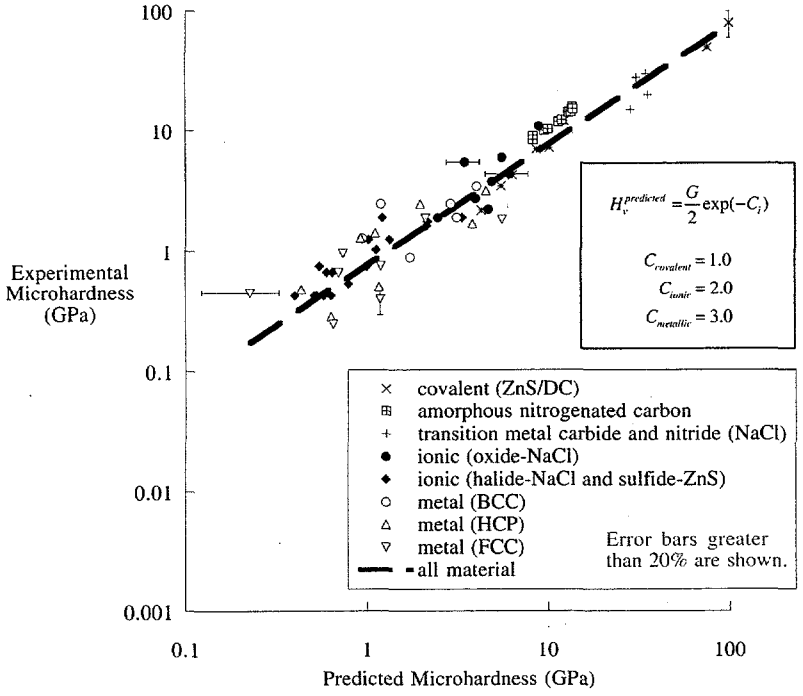

Figure 1.2: Log-log plot of bulk hardness as a function of a two-parameter curve fit for 3 different classes of materials.

fcc metals and the transition metal carbides and nitrides, this model also works relatively well.

This section has shown that hardness scales very closely with elastic moduli for a given class of material. Appendix A shows how one can use scaling relationships between lattice constant and elastic moduli to design new hard materials.

1.3 Hardness of Metallic Carbonitrides

Upon closer examination, both the empirical model of hardness and the Huntington Peierls stress model break down in one very technologically important set of materials: the transition metal carbides and nitrides. All are interstitial compounds with identical crystal structures and slip systems. Although the incorporation of Poisson's ratio differences in the Peierls stress does make a small difference, the mechanical hardnesses of ZrN and TiN are significantly less than ZrC and TiC despite comparable values of the shear modulus and Huntington Peierls stress (see Fig. 1.4).

Table 1.4: Values of h and b for various crystal structures.

Structure	h	b	h/b
dc	$\{111\}/12$	$\langle 112\rangle/6$	0.353
ZnS	$\{111\}/12$	$\langle 112\rangle/6$	0.353
NaCl	$\{110\}/2$	$\langle 110\rangle$	0.500
hcp[a]	–	–	0.720
bcc	$\{110\}/2$	$\langle 111\rangle/2$	0.816
fcc	$\{111\}/3$	$\langle 112\rangle/6$	1.414

[a]Table 1.3 and Fig. 1.3 use this value of h/b which was taken from Ref. [28]. For the hcp metals, a value of approximately 1.414 is more appropriate and will shift the hcp metals into the fcc scatter band, but this will not change the conclusions of this chapter.

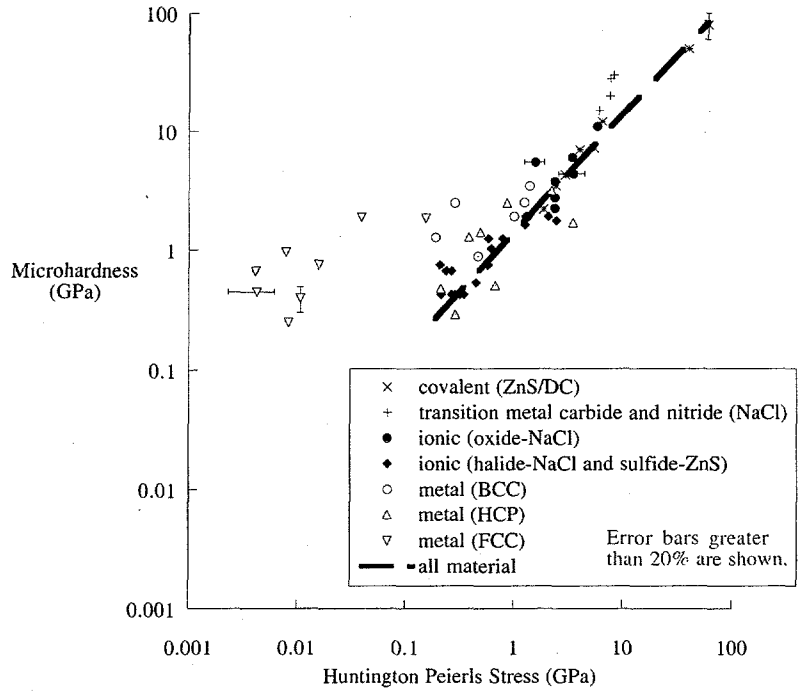

Figure 1.3: Log-log plot of bulk hardness as a function of the Huntington Peierls stress for 3 different classes of materials.

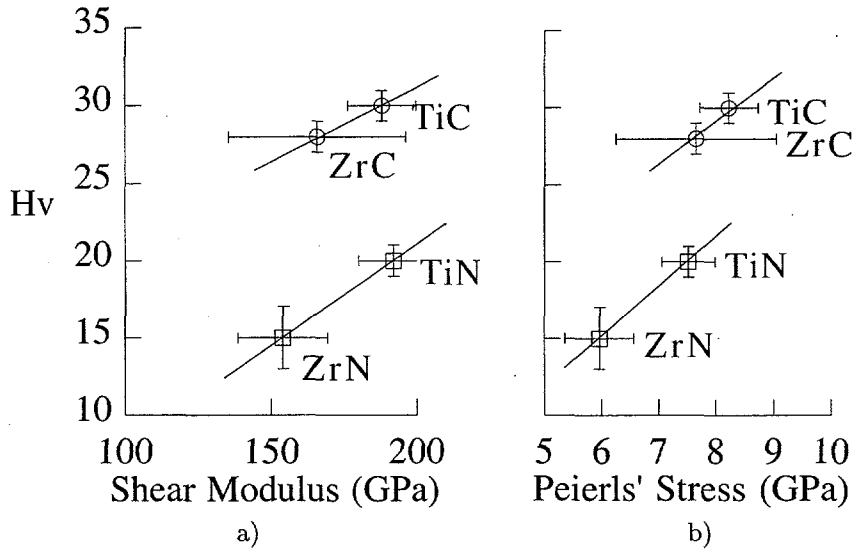

Figure 1.4: Plots of bulk hardness as a function of shear modulus and Huntington Peierls stress for TiC, TiN, ZrC & ZrN.

The simplest possible extension to the Huntington model of Peierls stress is to incorporate a more accurate periodic restoring force along the slip plane. The sinusoidal form of the restoring force was originally chosen because it made the problem mathematically tractable and because there were few physical measurements of non-linear elastic constants available at the time. Foreman [29] first treated this problem analytically in 1951, and Bullough [30] offers a more recent formulations.

Because this research was done in collaboration with the condensed matter theory research groups of Professors Marvin Cohen and Steven Louie, we tried to identify a method of calculating the restoring force on a dislocation using *ab initio* atomistic computational techniques. The Peierls formulation requires only the force–displacement curve obtained when two rigid half planes of material are given a relative displacement along the slip direction. This curve can be calculated from first-principles by taking two blocks of atoms and calculating the total energy and internal stresses for a series of rigid displacements. In order to avoid surface effects, one will actually calculate the energy and stress for an array of slabs. As the slab thickness is increased, the force energy curve will converge quickly to the solution of two infinite half planes.

Unfortunately, there is no natural way to constrain the deformation to be localized between two specific planes. It is computationally simple to fix all of the atom positions, but this technique is physically unrealistic because the elasticity solution for a straight edge dislocation has displacements both in the

direction of slip and normal to the slip plane. However, if you allow freedom for the slabs to relax in the direction of slip, your crystal will relax all the way back to the unstrained configuration. Any type of intermediate constrain would require *a priori* knowledge of the deformation field.

A more natural measure of a crystal's resistance to shear is to perform a stress controlled experiment and to allow all strains orthogonal to the applied stress to relax. To calculate the Peierls stress in this manner would require a simulation cell with a dislocation inside of it. Since dislocations actually move by kink migration, a full three-dimensional calculation of 1000 atoms or more is needed. This is currently at the upper limit of what can be done using *ab initio* techniques with the best computers in the world. A much easier, but still non-trivial, computation is to measure a crystal's resistance to fully relaxed simple shear. The maximum stress that a crystal can resist is the ideal shear strength of the crystal, and this strength sets an upper bound on the mechanical strength a material can have.

Ideal strengths are of interest in their own right, and may be sufficient to explain the differences in hardness between TiC and TiN. The stress–strain curves from the ideal strength experiments also can be incorporated into a more general Peierls stress formulation.

1.4 Conclusion

A two-parameter curve fit or a simple Peierls-stress model describes the room temperature hardness of a wide variety of materials. However, these models do not account for the differences in hardness between the transition metal carbides and nitrides. Accurate electronic structure calculations of the nonlinear elastic behavior of TiC and TiN are proposed in an attempt to explain the high hardnesses of the transition metal carbides.

Chapter 2

The Ideal Shear Strengths of Al and Cu[†]

2.1 Introduction

Let a hypothetical, defect-free crystal be loaded until the lattice itself becomes unstable and the crystal spontaneously deforms or breaks. The stress at elastic instability is the "ideal strength" [34]. The ideal strength is scientifically interesting for at least four reasons [35].

First, the ideal strength sets an upper bound on the strength the material can have. While it may not be possible to achieve the ideal strength in practice, it is not possible to exceed it. There is both scientific and engineering value in knowing the limits on what can be done.

Second, the ideal strength can be calculated *ab initio* for elemental solids and ordered compounds. The upper limit of strength is, therefore, one of a small number of problems in the mechanical behavior of materials that can actually be solved from first principles.

Third, the ideal strength is approached in situations that are technologically relevant. These include the low-temperature deformation of "inherently strong" materials, such as diamond, Si, Ge, and, possibly, some of the transition-metal carbonitrides, and also includes the nanoindentation of materials with low defect densities.

Fourth, the ideal strength is an inherent material property. Understanding its source and characteristics can help identify those aspects of mechanical behavior that are fundamental consequences of crystal structure and bonding.

Since the ideal strength is determined by elastic instability, the possibility of calculating it has, in theory, been available since the development of the pseudopotential theory made *ab initio* elasticity calculations practical [36]. However, substantial computational resources are required, and, until recently,

[†]The material in this chapter is a combination of the research in Refs. [31–33].

the calculations that were done were limited to tensile deformation along axes of high symmetry [37–39] or shear deformation in simple (unrelaxed) shear [40–42]. These constraints are unphysical, will always increase the predicted shear strength, and may produce significant overestimates. It is now practical to find the elastic limits for shear as well as for tensile deformation under fully relaxed conditions [31, 32].

This chapter presents *ab initio* calculations of the ideal shear strengths of Al and Cu. We also discuss the similarities and differences in the large-strain elastic behavior of Al and Cu. In the fully relaxed case, the two have very similar strengths (when these are expressed in dimensionless form), but very different relaxation strains.

2.2 Method of Calculation

The total energies of Al and Cu are computed as a function of strain using the LDA pseudopotential total-energy scheme with a plane-wave basis set [36, 43–46]. The pseudopotential for Cu was generated including semi-relativistic corrections [47], while the pseudopotential for Al was constructed without relativistic corrections [48]. We used a cut-off energy of 40 Ry for Al and 70 Ry for Cu. A grid of 2400 k points was used for Al. A grid of 1300 k points was used for Cu. These choices ensure convergence to less than 1 mRy (0.013 eV) per atom.

The shear stress is found by straining the crystal in a series of incremental simple shears, calculating the energy and volume as functions of the strain, and taking the derivative of the energy with respect to the strain. The ideal shear strength (in the low-temperature limit) is the maximum value of this stress. In both Al and Cu the shear strength is minimum for shear on a $\{111\}$ plane in a $\langle 112\rangle$ direction. It is, therefore, useful to refer the displacements to a Cartesian coordinate system with a unit vector, $\boldsymbol{e_3}$, perpendicular to the (111) plane and unit vectors $\boldsymbol{e_1}$ and $\boldsymbol{e_2}$ parallel to the $[11\bar{2}]$ and $[1\bar{1}0]$ directions, respectively (Fig. 2.1a). With this notation, an incremental simple shear in the $[11\bar{2}]$ direction on (111) takes the form

$$\delta\boldsymbol{\epsilon} = \epsilon_{13}(\boldsymbol{e_1}\boldsymbol{e_3} + \boldsymbol{e_3}\boldsymbol{e_1}). \tag{2.1}$$

To increment the strain under fully relaxed conditions, we impose $\epsilon_{13}(=\epsilon_{31})$, and adjust the other components of the strain tensor until their associated stresses vanish (specifically, until the calculated Hellman-Feynman stresses are < 0.05 GPa). Since $\epsilon_{12} = \epsilon_{23} = 0$ by symmetry, the relaxation strains are stretches along the coordinate axes.

While there is no unique definition of finite strain [49], the three lattice parameters, $\boldsymbol{a^\alpha}$, are defined at each step of the deformation and can be described by the three functions, $\boldsymbol{a^\alpha}(n)$, where n is the number of incremental strain steps in the simulation. $\boldsymbol{a^\alpha}(0)$ represents the unstrained lattice. If $\boldsymbol{D}(n,m)$ is the Cartesian tensor that describes the deformation between steps m and n,

$$a_i^\alpha(n) = a_i^\alpha(m) + D_{ij}(n,m)a_j^\alpha(m). \tag{2.2}$$

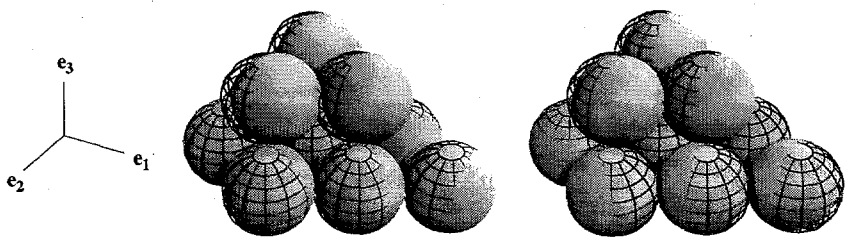

Figure 2.1: Illustration of the atomic arrangement before and after unrelaxed shear in Al and Cu. The cages give the original atom positions in the fcc lattice, the solid spheres show atom positions at the point of shear instability. The Cartesian coordinate system is illustrated at left: $\{\boldsymbol{e_1}, \boldsymbol{e_2}, \boldsymbol{e_3}\} = \{[11\bar{2}], [1\bar{1}0], [111]\}$

Given $\boldsymbol{D}(n, m)$, the true strain, ϵ, and the engineering strain, ϵ^E, are defined by

$$\epsilon_{ij}(n) = \frac{1}{2} \sum_{m=1}^{n} [D_{ij}(m, m-1) + D_{ji}(m, m-1)] \tag{2.3}$$

and

$$\epsilon^E_{ij}(n) = \frac{1}{2}[D_{ij}(n, 0) + D_{ji}(n, 0)]. \tag{2.4}$$

The derivatives of the energy with respect to the true strain define the stresses that drive incremental deformation, and, therefore, the true strain is used to calculate the stress.

The energy is a unique function of the strain, ϵ_{13}, when either: (1) the crystal is unrelaxed, so ϵ_{13} is the only non-zero strain, or (2) the crystal is fully relaxed, so setting the value of ϵ_{13} fixes *all* the other strains. In either case, the conjugate shear stress is

$$\tau = \sigma_{13} = \frac{1}{V} \frac{\partial E}{\partial \epsilon_{13}} = \frac{1}{V} \frac{\partial E}{\partial \gamma_{13}}, \tag{2.5}$$

where $\gamma_{ij} = \epsilon_{ij} + \epsilon_{ji} = 2\epsilon_{ij}$ is the shear, and V is the atomic volume at the applied strain. The relevant shear modulus, G', is determined by the second derivative, $\partial^2 E / \partial \gamma^2$. For shear in the $[11\bar{2}]$ direction on the (111) plane of fcc, the shear moduli are

$$G'_u = C'_{55} = \frac{1}{3}[c_{11} + c_{44} - c_{12}] \text{ and} \tag{2.6}$$

$$G'_r = \frac{1}{s'_{55}} = \frac{3\, c_{44}(c_{11} - c_{12})}{4\, c_{44} + c_{11} - c_{12}}, \tag{2.7}$$

Table 2.1: Calculated and experimental lattice parameters and elastic moduli for Al and Cu.

	Al		Cu	
	calc.	exp.	calc.	exp.
lattice constant (Å)[a]	4.12	4.05	3.57	3.61
G'_r (GPa[b]	22 ± 3	24.5	30 ± 4	30.5
G'_u (GPa)[b]	27 ± 3	24.8	40 ± 4	40.8

[a]Experimental values from Ref. [11].
[b]Shear moduli are defined by Equations (2.6) and (2.7). Experimental Voigt elastic constants are from Ref. [10].

where G'_u governs the unrelaxed case, where $\epsilon_{ij} = 0$ unless $ij = 13$ or 31 (=5 in the Voigt notation), G'_r governs the relaxed case, $\sigma_{ij} = 0$ unless $ij = 13$ or 31, the c_{ij} are the Voigt elastic constants for the cubic crystal, and c' and s' are, respectively, the Voigt elastic constants and compliances in the coordinate system shown in Fig. 2.1. The moduli govern incremental displacements from the current state and are, hence, functions of the strain.

2.3 Results

The results of the calculations are summarized in Tables 2.1–2.3 and in Figs. 2.2 and 2.3. Table 2.1 compares the calculated and experimental values for the lattice constants and shear moduli at zero applied strain. The close agreement indicates the relative accuracy of the calculations.

However, the fact that the computed lattice constant of Al is larger than the experimental value indicates a slight problem with the pseudopotential chosen. For metals, the local density approximation to density functional theory should always results in some degree of "overbinding": lattice constants are smaller and bulk moduli are higher than experiment. [50] The computed lattice constants in other LDA *ab initio* studies of Al at 0 K range from 3.97 Å to 4.01 Å [39, 51, 52]. All are smaller than the experimental value.

Fortunately, the small error in the pseudopotential is not likely to affect the conclusions of this chapter significantly. The error does produce systematic "underbinding" in Al. The calculated bulk modulus (71 GPa) is 10% smaller than the experimental value (77 GPa [10]). Errors in the computed ideal strength will be significantly smaller than the error in elastic moduli because the strength is determined from the first derivative with respect to strain, while the moduli are determined from the second derivative of energy with respect to strain. Errors in the slope of a smooth function are always smaller than errors in curvature. The magnitude and direction of the atomic relaxation also should not be affected greatly by the error in the pseudopotential.

Figure 2.2 shows the energy of Al and Cu as a function of the shear strain,

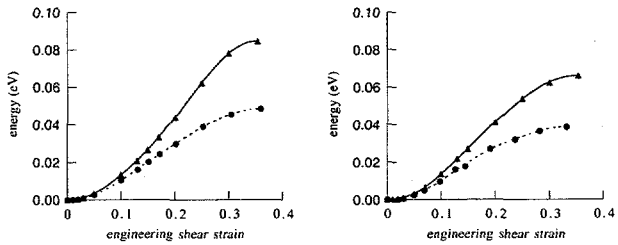

Figure 2.2: a) Aluminum and b) copper energy versus engineering strain for both the unrelaxed (▲'s and smooth fit) and relaxed (●'s and dashed fit) cases.

$E(\gamma)$, computed both with and without relaxation, and figure 2.3 plots the stress-strain curves, $\tau(\gamma)$, for the two materials studied in the fully relaxed case. The stresses and strains at instability are tabulated in Tables 2.2 and 2.3. The results show the importance of elastic relaxation, which decreases the shear strength some 40% from the unrelaxed value. Interestingly, the normalized shear strengths of Al and Cu in the fully relaxed state are essentially identical ($0.085G'_r$) and are much closer to the classic Frenkel estimate ($0.1\,G$) than to the more modern estimates that have been preferred in recent years [34].

Unfortunately, there are no directly comparable experimental data known to us. The calculations relate, strictly, to perfect crystals in the limit of zero temperature. There are no data known to us on dislocation-free Al, but Brenner [53] did measure the strength of nominally dislocation-free Cu whiskers. He found a tensile yield strength of 2.9 GPa for tension along $\langle 111 \rangle$, which translates into a critical resolved shear stress, τ_c, of 0.82 GPa ($0.027\ G'_r$) for slip on the $\{111\}$ plane in the $\langle 112 \rangle$ direction. Brenner's measurements were done at room temperature, so the strength must be corrected to 0 K. While there is no exact way to do this, a crude model described by Kelly and Macmillan [34] suggests that $\tau_c(0) \approx 2.5\tau_c(273)$ is not a bad estimate. Using this approximation, we project $\tau_c \approx 1.1$ GPa at 273 K, which is not unreasonable in light of the Brenner result. A better test can be made by computing the strength of high-melting-point materials, which should show a much smaller thermal effect. This is done in Chapter 4.

The elastic strain at shear instability is tabulated in Table 2.3. The imposed shear is γ_{13}, a displacement of the (111) planes in the $[11\bar{2}]$ direction. The relaxation strains are the stretches, ϵ_{11} and ϵ_{22} in the (111) plane, and ϵ_{33} perpendicular to it. The primary shear strain (γ^E_{13}) at instability is nearly the same for Al and Cu (Table 2.3), and is significantly below the value (17.8%) that a rigid-ball model would produce.

However, the relaxation strains in the two cases (Fig. 2.1) are dramatically different. Cu is relaxed by a shear in the (111) plane in which a contraction in the

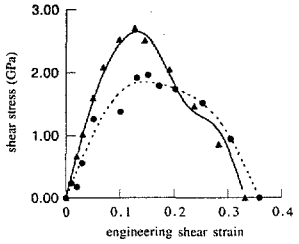

Figure 2.3: Stress versus engineering strain for Cu (▲'s and smooth fit) and Al (●'s and dashed fit). The data points are the calculated Hellman-Feynman stresses and the smooth curves are the derivatives of the smooth fits to the energies.

Table 2.2: Ideal shear strengths with and without structural relaxations.

	failure stress		
	$\tau^r_{\max}$ (GPa)	$\tau^r_{\max}/G'_r$	$\tau^u_{\max}$ (GPa)
Al	1.85 ± 0.1	0.084	3.4 ± 0.1
Cu	2.65 ± 0.2	0.088	4.0 ± 0.1

Table 2.3: Engineering strains at shear instability

	failure strain (%)				
	γ^E_{13}	ϵ^E_{11}	ϵ^E_{22}	ϵ^E_{33}	$\Delta V/V$
Al	14.5	1	−3	3	1.4
Cu	13	−3	3	0.2	0.4

direction of shear displacement (ϵ_{11}) is balanced by a perpendicular expansion (ϵ_{22}). The separation between (111) planes is almost unchanged (ϵ_{33} small), so the volume is almost constant. Al, on the other hand, is relaxed primarily by a shear in the $(11\bar{2})$ plane, with $\epsilon_{33} \cong -\epsilon_{22} > \epsilon_{11}$. The (111) interplanar spacing increases by $\approx$ 3%, and the volume increases by 1.4%.

2.4 Discussion

Both the similarities and differences in the behavior of Al and Cu merit discussion. The most striking similarities are the crystallography of the shear that produces minimum strength (the weak direction in both Al and Cu is in the $\langle 112 \rangle$ direction in a $\{111\}$ plane) and the virtual identity of the normalized shear strengths. The most striking dissimilarity is the qualitative difference in the relaxation strain.

2.4.1 The soft direction in shear

A shear in a $\langle 112 \rangle$ direction in a $\{111\}$ plane in a material with the fcc crystal structure is a shear that is associated with twinning in $\{111\}$ and with the partial slip at the boundary of a stacking fault in $\{111\}$. Hence one would expect this shear to be the soft shear in materials like Cu that twin and form stacking faults. However, Al has a high stacking fault energy, and one might expect some other shear to be preferred. The reason that $\langle 112 \rangle \{111\}$ is the soft shear in Al can be explained by the fact that the applied shear is uniform and the local atomic coordination near the instability resembles that of the relaxed crystal more than that of a twinned or faulted one.

If a perfect crystal of Al were strained beyond its shear instability, the instability would necessarily resolve itself in a shower of dislocations, twins or stacking faults, whichever were easier to achieve. It is at this point that the choice between total dislocations, partial dislocations or twins would be made. Since even a small shear carries elastic energy equivalent to that of a high density of dislocations, the elastic energy of a crystal strained to instability is sufficient to carry it into whatever defect state is preferred.

2.4.2 The normalized shear strength

The close similarity between the normalized shear strengths of Al and Cu is probably fortuitous. The unrelaxed shear strengths are not that close ($\approx 0.13G'_u$ for Al versus $\approx 0.1G'_u$ for Cu) and the relaxation patterns are very different. Nonetheless, since our preliminary calculations for W also produce a shear strength near $0.085G'_r$, this appears to be a common value for the ideal shear strength of a metal.

2.4.3 The relaxation strain

Detailed electronic structure calculations will be conducted in the near future to examine the effects of the d electron core on the bonding of Cu and to determine whether the presence of a d core can explain the dramatic differences in the relaxation behaviors of Al and Cu. However, these differences can be explained, qualitatively, from their elastic behavior. To phrase this discussion, we first present the Voigt compliance tensors (Eq. (2.8) and (2.9)) for Al and Cu in the form they take after transformation into the coordinate system shown in Fig. 2.1:

$$s'_{\mathrm{Al}}(\epsilon=0)=\begin{bmatrix} 0.0139 & -0.0051 & -0.0045 & 0 & -0.0019 & 0 \\ -0.0051 & 0.0139 & -0.0045 & 0 & 0.0019 & 0 \\ -0.0045 & -0.0045 & 0.0132 & 0 & 0 & 0 \\ 0 & 0 & 0 & 0.0408 & 0 & 0.0038 \\ -0.0019 & 0.0019 & 0 & 0 & 0.0408 & 0 \\ 0 & 0 & 0 & 0.0038 & 0 & 0.0380 \end{bmatrix} \mathrm{GPa}^{-1} \tag{2.8}$$

$$s'_{\mathrm{Cu}}(\epsilon=0)=\begin{bmatrix} 0.0077 & -0.0038 & -0.0014 & 0 & -0.0069 & 0 \\ -0.0038 & 0.0077 & -0.0014 & 0 & 0.0069 & 0 \\ -0.0014 & -0.0014 & 0.0052 & 0 & 0 & 0 \\ 0 & 0 & 0 & 0.0328 & 0 & 0.0138 \\ -0.0069 & 0.0069 & 0 & 0 & 0.0328 & 0 \\ 0 & 0 & 0 & 0.0138 & 0 & 0.0230 \end{bmatrix} \mathrm{GPa}^{-1} \tag{2.9}$$

Since the [111] direction is a three-fold symmetry axis in fcc, the compliance tensor has a superficially trigonal symmetry; the non-diagonal elements s'_{15} and s'_{25} do not ordinarily vanish. However, $s'_{15} = -s'_{25}$ and, since $s'_{35} = 0$, the imposition of a shear stress in the $[11\bar{2}]$ direction on (111), which is τ_{13} (or t_5 in the Voigt notation) produces a shear of type $[11\bar{2}](111)$ that is relaxed by a shear in the (111) plane, $\epsilon_{11} = -\epsilon_{22}$, of precisely the type that is dominant in Cu (Table 2.3). However, the value of s'_{15} is determined by the elastic anisotropy factor, Δ $(= (c_{11} - c_{12} - 2\,c_{44})/c_{44})$, according to the relation

$$s'_{15} = \frac{\Delta}{3\sqrt{2}(c_{11}-c_{12})c_{44}}. \tag{2.10}$$

It follows that s'_{15} increases with Δ, and vanishes when $\Delta = 0$. The strong elastic anisotropy of Cu has the consequence that its elastic, in-plane relaxation is much greater than that in the more isotropic Al.

A shear of type $[11\bar{2}](111)$ breaks the symmetry of the fcc crystal. The symmetry of the strained crystal allows $s'_{15} \neq -s'_{25}$ and $s'_{35} \neq 0$, so there can be a relaxation strain, ϵ_{33}, perpendicular to the (111) plane and a net volume change. The symmetry change is exploited very quickly in the almost isotropic Al crystal, which rapidly develops significant values of ϵ_{33}, $\epsilon_{11} + \epsilon_{22}$, and ΔV. In the anisotropic Cu crystal, in contrast, the finite-strain effect is small, and

the relaxation strain is only slightly perturbed from its symmetry in the relaxed state.

The qualitative difference between the relaxation strains of Al and Cu is also observed experimentally. Approximate compliance tensors of Al and Cu at the shear instability are presented below (Eq. (2.11) and (2.12)), as estimated from the third-order elastic constants tabulated in [10]. Even though the experimental data were taken at strains of only a fraction of a percent, the measured third order elastic constants do predict that the s'_{15} and s'_{25} compliances of Al will change sign. The compliances also predict the relative magnitudes and sign of the relaxations in Al, and the signs of the relaxations in Cu. Finally, one can extract estimates of the sign and magnitude of the volume change with applied shear by summing s'_{15}, s'_{25} and s'_{35}. For Al, the volumetric compliance is 1.4% and for Cu, 0.8%. These figures are again qualitatively consistent with the theoretical results given in Table 2.3.

$$s'_{\mathrm{Al}}(\epsilon = 0.15) = \begin{bmatrix} 0.0135 & -0.0055 & -0.0027 & 0 & 0.0026 & 0 \\ -0.0055 & 0.0154 & -0.0072 & 0 & -0.0063 & 0 \\ -0.0027 & -0.0072 & 0.0176 & 0 & 0.0177 & 0 \\ 0 & 0 & 0 & 0.0353 & 0 & 0.0092 \\ 0.0026 & -0.0063 & 0.0177 & 0 & 0.0730 & 0 \\ 0 & 0 & 0 & 0.0092 & 0 & 0.0394 \end{bmatrix} \mathrm{GPa}^{-1} \tag{2.11}$$

$$s'_{\mathrm{Cu}}(\epsilon = 0.13) = \begin{bmatrix} 0.0087 & -0.0046 & -0.0027 & 0 & -0.0128 & 0 \\ -0.0046 & 0.0083 & -0.0004 & 0 & 0.0109 & 0 \\ -0.0027 & -0.0004 & 0.0067 & 0 & 0.0097 & 0 \\ 0 & 0 & 0 & 0.0239 & 0 & 0.0109 \\ -0.0128 & 0.0109 & 0.0097 & 0 & 0.0680 & 0 \\ 0 & 0 & 0 & 0.0109 & 0 & 0.0217 \end{bmatrix} \mathrm{GPa}^{-1} \tag{2.12}$$

2.5 Conclusion

We have calculated the ideal shear strengths of aluminum and copper using pseudopotential density functional theory. Structural relaxations orthogonal to the applied shear significantly reduce the values of ideal shear strength, resulting in strengths of 8–9 percent of the shear modulus for both Al and Cu. However, the geometry of the relaxations in Al and Cu is very different. To some degree, this can be explained using experimentally measured third order elastic constants.

Chapter 3

The Internal Stability of an Elastic Solid[†]

3.1 Introduction

Chapter 2 presented, to this author's knowledge, the first fully relaxed *ab initio* calculations of ideal shear strength in any material and showed the importance of structural relaxations orthogonal to the applied shear. Our calculations also revealed that the values of ideal strength were sensitive to the finite strain measure used to determine the stresses by differentiation. Before continuing our computational research, we decided to rigorously examine how the thermodynamic conditions of elastic stability apply to calculations of ideal strength.

It is sometimes useful to think of ordinary plastic deformation as a structural instability, in which elastic stress drives a locally stable parent "phase" into an instability that can only be resolved by creating or reconfiguring defects such as dislocations, or by transforming to a new crystal structure. This perspective is most natural when the parent phase contains no mobile defects and the deformation is triggered by a stress so large that the lattice itself becomes unstable. This elastic limit sets an upper bound on the mechanical strength a material can have. Given recent advances in theoretical methods and computing machines it is possible to calculate the elastic limits of real materials with considerable accuracy, including both the theoretical stress and the detailed nature of the atomic rearrangements as the elastic limit is approached [31, 32, 37, 39–41].

Despite periodic investigations over many years, however, the basic thermodynamic criteria that govern elastic stability are not entirely clear [34, 55–59]. This creates an uncertainty in how first-principles calculations or simulations ought to be done, and what their results have to say about the true limits of strength. Even in the simplest case, homogeneous, quasistatic elastic deformation to failure, some clarification is needed in at least three separate areas: the

[†]The research presented in this chapter has been accepted for publication in *Phil. Mag. A* (Ref. [54].)

thermodynamic conditions for stability, the conditions of stability under load control, and the most efficient approach to first-principles calculations.

The first problem concerns the conditions of stability. The analysis of elastic stability is complicated by the fact that the states of interest are subject to finite stresses and strains that change their symmetry and affect their mechanics. Recent investigations of this subject [56–59] have begun from the perspective of continuum mechanics and used the stability criterion

$$\delta F \geq \delta W, \tag{3.1}$$

which assumes fixed temperature and requires that the increment to the Helmholtz free energy in any real or virtual displacement equal or exceed the mechanical work done by the applied stresses. The ambiguity in this approach [56] lies in the nature of the mechanical work, which is done by some loading mechanism that functions as a thermodynamic reservoir. To apply the stability criterion the work must be evaluated to second order. While the various convenient measures of the applied stress, for example, the Cauchy stress in real space and the stress that is conjugate to the Lagrangian strain, have equivalent first-order effects, they differ in the second order. As Hill [56] and Hill and Milstein [57] point out, this has the consequence that the limit of strength changes with the nature of the stress that is maintained by the reservoir. Recent investigations [39, 58, 59] avoid this ambiguity by assuming that the Cauchy stresses are controlled, and Wang *et al.* [59] use this condition to define a path-dependent "Gibbs integral" that has the local features of the Gibbs free energy. But it is not completely clear why this choice is more fundamental than any of several others, particularly since it is not easy to design mechanisms that control the Cauchy stress to second order.

The second problem concerns the conditions of stability for deformation under mixed stress and strain control. In particular, the limit of strength that is ordinarily of greatest interest is the strength under uniaxial stretch or simple shear, with all other stresses fully relaxed. In this case the governing thermodynamic potential includes only one strain variable and has only one modulus, and one needs to know how the limit of stability determined by that modulus relates to those that apply under more general conditions.

The third problem is the practical problem of finding the relevant limits of strength by direct, *ab initio* calculations. Since these calculations are computationally expensive, it is important to obtain the desired information in the most efficient possible way. In particular, it is critical to know how the instabilities that are captured in the calculations relate to those identified by the thermodynamic criteria, and whether the details of the calculations cause important instabilities to be miscalculated or missed entirely.

To investigate these questions we return to Gibbs' original formulation of the conditions of stability [60] and apply the method to a homogeneous, elastic solid under finite strain. Gibbs' conditions govern internal stability and enforce the requirement that the system be stable with respect to arbitrary reconfigurations that do not alter its boundaries. They are, therefore, independent of the nature

of the external loads or the mechanisms that hold the boundaries in place. As we shall see, the conditions of internal elastic stability are identical to those derived from Eq. (3.1) when the loading mechanism fixes the Cauchy stress [59]. Hence, the conditions of stability based on the Cauchy stress always apply. Other loading mechanisms may introduce other conditions, which may be more stringent, but cannot obviate these conditions of internal stability.

We then consider the conditions of stability under uniaxial deformation or simple shear. In this case the conditions of stability relate to the single surviving modulus. No new conditions of stability are added, but the conditions of internal stability must still be obeyed, and instabilities that result from deformations orthogonal to the chosen deformation may be missed.

Finally, we consider how to calculate the limits of stability and, in particular, whether it is possible to obtain reasonable answers without computing the full matrix of elastic moduli after each increment of elastic deformation.

3.2 The Conditions of Internal Equilibrium†

We use the notation employed by Eringen [61], with minor variations that should be clear from context. A strained solid is described by the relations

$$x_k = \tilde{x}_k(X_k) \qquad\qquad X_K = \tilde{X}_K(x_k), \tag{3.2}$$

where the x_k are coordinates in the current state (the "spatial" or "Eulerian" frame), the X_K are coordinates in a convenient reference state (the "material" or "Lagrangian" frame), and both sets of coordinates are Cartesian. The differentials of Eq. (3.2) are the "deformation gradients", $x_{k,K}$ and $X_{K,k}$:

$$dx_k = x_{k,K} dX_K \qquad\qquad dX_K = X_{K,k} dx_k. \tag{3.3}$$

Defining the displacement vector, $\boldsymbol{u}$, such that $\boldsymbol{x} = \boldsymbol{X} + \boldsymbol{u}$,

$$x_{k,K} = \delta_{kK} + \delta_{kL} U_{L,K} \qquad\qquad X_{K,k} = \delta_{kK} + \delta_{lK} u_{l,k}, \tag{3.4}$$

where U_K and u_k are, respectively, the components of $\boldsymbol{u}$ in the material and spatial frames, $U_{L,K}$ and $u_{l,k}$ are the displacement gradients in the two frames, and the $\delta_{kK} (= e_k \cdot e_K)$ are the "shifters" that relate unit vectors along the material and spatial coordinates axes (they are Kronecker $\boldsymbol{\delta}$'s when the coordinate axes coincide).

The strain is ordinarily measured by the Lagrangian (Green's) strain, a tensor in the material frame whose elements are

$$E_{KL} = \frac{1}{2}[x_{k,K} x_{k,L} - \delta_{KL}] = \frac{1}{2}[U_{K,L} + U_{L,K} + U_{P,K} U_{P,L}] = E_{LK}, \tag{3.5}$$

†This derivation is the work of J. W. Morris Jr., but it is included here to provide context for the following discussion and the following chapter.

or by the Eulerian strain, the complementary strain measure in the current frame:

$$e_{kl} = \frac{1}{2}[\delta_{kl} - X_{K,k}X_{K,l}] = \frac{1}{2}[u_{k,l} + u_{l,k} + u_{p,k}u_{p,l}] = e_{lk}. \tag{3.6}$$

The two strain measures are connected by the relation

$$E_{KL} = x_{k,K}x_{l,L}e_{kl}. \tag{3.7}$$

When the displacement gradients are small ($u_{k,l} = \delta u_{k,l}$) both strain measures reduce to the linear strain,

$$\epsilon_{kl} = \frac{1}{2}[u_{k,l} + u_{l,k}]. \tag{3.8}$$

However, when the displacement gradients are finite, both the strain measures and their increments differ. In particular, if the material points are given the small displacements, $\boldsymbol{\delta u}$, from their present positions [62],

$$\delta E_{KL} = x_{k,K}x_{l,L}\left[\frac{1}{2}(\delta u_{k,l} + \delta u_{l,k})\right] = x_{k,K}x_{l,L}\delta\epsilon_{kl}. \tag{3.9}$$

We seek the conditions that are necessary for internal equilibrium. Let the solid have a fixed temperature and composition, and a homogeneous mechanical state that is controlled by its external surface ("strain control"). Its mechanical equilibrium is, then, governed by the Helmholtz free energy, which must have at least a local minimum value with respect to reconfigurations that keep the boundary fixed. To phrase this condition mathematically, let the material particle, $\boldsymbol{X}$, that is currently located at the position, $\boldsymbol{x}$, within the volume, V, of the body be given the small displacement, $\boldsymbol{\delta u}(\boldsymbol{x})$, whose values form a differentiable field over V. Equilibrium requires that

$$\delta F[\boldsymbol{\delta u}(\boldsymbol{x})] \geq 0, \tag{3.10}$$

where the variation is taken at constant temperature and composition and the only displacements that are permitted are those that leave the boundary unchanged.

The boundary constraint can be incorporated into the condition (3.10) by the method of Lagrange multipliers, giving the equivalent condition [63],

$$\delta F[\boldsymbol{\delta u}(\boldsymbol{x})] - \int_S t_{ij}\delta u_i n_j dS \geq 0, \tag{3.11}$$

where the t_{ij} are constant Lagrange multipliers, $\boldsymbol{\delta u}$ is the variational displacement of the boundary element, dS, whose normal is $\boldsymbol{n}$, and $\boldsymbol{\delta u}(\boldsymbol{x})$ can now be any differentiable vector field over V. Via the divergence theorem,

$$\begin{aligned}\delta F[\boldsymbol{\delta u}(\boldsymbol{x})] - \int_S t_{ij}\delta u_i n_j dS &= \delta F[\boldsymbol{\delta u}(\boldsymbol{x})] - \int_v t_{ij}\delta u_{i,j} dV \\ &= \delta F[\boldsymbol{\delta u}(\boldsymbol{x})] - \int_S t_{ij}(\delta\epsilon_{ij} + \delta\omega_{ij}) dV \geq 0,\end{aligned} \tag{3.12}$$

where $\delta\epsilon_{ij} = \frac{1}{2}(\delta u_{i,j} + \delta u_{j,i})$ is the incremental strain, and $\delta\omega_{ij} = \frac{1}{2}(\delta u_{i,j} - \delta u_{j,i})$ is the incremental rotation.

The variation in the Helmholtz free energy is most easily evaluated in the reference state, $\boldsymbol{X}$, which has the fixed volume, V^0:

$$\begin{aligned}\delta F[\boldsymbol{\delta u}(\boldsymbol{x})] &= \int_{V^0} \left[\frac{\partial F_{V^0}}{\partial E_{KL}}\right] \delta E_{KL} dV^0 \\ &= \int_V \frac{\rho}{\rho_0} \left[\frac{\partial F_{V^0}}{\partial E_{KL}}\right] x_{k,K} x_{l,L} \delta\epsilon_{kl} dV,\end{aligned} \tag{3.13}$$

where $\boldsymbol{\delta E}$ is the increment to the Lagrangian strain, and we have used Eq. (3.9) and the identity $\rho dV = \rho_0 dV^0$ to transform the integral into the current frame. Inserting (3.12) into (3.9), the condition of mechanical equilibrium can be written

$$\int_V \left\{ \left[\frac{\rho}{\rho_0}\left[\frac{\partial F_{V^0}}{\partial E_{KL}}\right] x_{k,K} x_{l,L} - t_{kl}\right] \epsilon_{kl} - t_{kl}\delta\omega_{kl} \right\} dV \geq 0. \tag{3.14}$$

The condition (3.14) holds for arbitrary $\delta u_{i,j}$ only if

$$t_{ij} = t_{ji} \tag{3.15}$$

and

$$t_{kl} = \frac{\rho}{\rho_0}\left[\frac{\partial F_{V^0}}{\partial E_{KL}}\right]\left[\frac{1}{2}(x_{k,K}x_{l,L} + x_{l,K}x_{k,L})\right]. \tag{3.16}$$

Equation (3.16) is, in fact, the thermodynamic definition of the Cauchy stress [61], and establishes that our multipliers are precisely the elements of the Cauchy stress tensor (as they must be [63]).

To find the conditions of mechanical stability we need to develop the variation of the free energy to the second order. The Helmholtz free energy of an elastic solid is usually and conveniently written as a function of the Lagrangian strain. For fixed composition the free energy density in the reference state is, to second order

$$F_{V^0}(\boldsymbol{E}, T) \cong F_{V^0}(T) + \tau_{KL}E_{KL} + \frac{1}{2}c_{KLMN}E_{KL}E_{MN}, \tag{3.17}$$

where V^0 is the volume in the reference state,

$$\tau_{KL} = \left[\frac{\partial \tilde{F}_{V^0}}{\partial E_{KL}}\right]_{E=0} \tag{3.18}$$

is the conjugate stress in the reference state, and

$$c_{KLMN} = \left[\frac{\partial^2 \tilde{F}_{V^0}}{\partial E_{KL}\partial E_{MN}}\right]_{E=0} \tag{3.19}$$

are the elastic moduli.

To first order in E, $x_{k,K} \cong \delta_{kK} + \delta_{kP}E_{PK}$. The variation of F_V^0 in an incremental strain is then, to second order,

$$\begin{aligned}\delta F_{V^0} &\cong [\tau_{KL}x_{k,K}x_{l,L} + c_{KLMN}E_{MN}\delta_{kK}\delta_{lL}]\,\delta\epsilon_{kl}\\ &= [\tau_{KL} + (\tau_{ML}\delta_{KN} + \tau_{KM}\delta_{LN} + c_{KLMN})E_{MN}]\,\delta_{kK}\delta_{lL}\delta\epsilon_{kl}\\ &= \Big\{\tau_{KL} + \Big[\frac{1}{2}(\tau_{ML}\delta_{KN} + \tau_{KM}\delta_{LN}\\ &\qquad + \tau_{NL}\delta_{KM} + \tau_{KN}\delta_{LM}) + c_{KLMN}\Big]E_{MN}\Big\}\delta_{kK}\delta_{lL}\delta\epsilon_{kl},\end{aligned} \tag{3.20}$$

where we have used the symmetry of the Lagrangian strain tensor, E_{KL}, and have also used the Voigt symmetry of the tensor of elastic moduli, c_{KLMN}. If we now multiply by the density ratio then, to second order,

$$\begin{aligned}\left[\frac{\rho}{\rho^0}\right]\delta F_{V^0} &= [1 - E_{PP}]\delta F_{V^0}\\ &\cong \{\tau_{KL} + B_{KLMN}E_{MN}\}\delta_{kK}\delta_{lL}\delta\epsilon_{kl},\end{aligned} \tag{3.21}$$

where the elements of the tensor

$$\begin{aligned}B_{KLMN} = \frac{1}{2}&(\tau_{ML}\delta_{KN} + \tau_{KM}\delta_{LN}\\ &+ \tau_{NL}\delta_{KM} + \tau_{KN}\delta_{LM} - 2\tau_{KL}\delta_{MN}) + c_{KLMN}\end{aligned} \tag{3.22}$$

are the moduli that govern the variation of the Cauchy stress with strain from a stressed reference state [64] (the form in Hill [56] is for the special case, $\rho = \rho_0$):

$$t_{kl} = \{\tau_{KL} + B_{KLMN}E_{MN}\}\delta_{kK}\delta_{lL}. \tag{3.23}$$

Note that $B_{KLMN} \neq B_{MNKL}$; the B_{KLMN} do not have full Voigt symmetry.

We are here concerned with the necessary conditions for stability on incremental strain from a stressed reference state. In this case,

$$E_{MN} = \delta E_{MN} = x_{m,M}x_{n,N}\delta\epsilon_{mn}, \tag{3.24}$$

so, to second order,

$$\left[\frac{\rho}{\rho^0}\right]\delta F_{V^0} = \frac{1}{V}\delta F \cong \tau_{kl}\delta\epsilon_{kl} + \lambda_{klmn}\delta\epsilon_{kl}\delta\epsilon_{mn}, \tag{3.25}$$

where V is the volume in the current configuration,

$$\tau_{kl} = \tau_{KL}\delta_{kK}\delta_{lL}, \tag{3.26}$$

and

$$\begin{aligned}\lambda_{klmn} &= \frac{1}{2}[B_{KLMN} + B_{MNKL}]\delta_{kK}\delta_{lL}\delta_{mM}\delta_{nN}\\ &= c_{klmn} + \frac{1}{2}[\tau_{km}\delta_{ln} + \tau_{kn}\delta_{lm} + \tau_{lm}\delta_{kn} + \tau_{ln}\delta_{km} - \tau_{kl}\delta_{mn} - \tau_{mn}\delta_{kl}],\end{aligned} \tag{3.27}$$

where $c_{klmn} = c_{KLMN}\delta_{kK}\delta_{lL}\delta_{mM}\delta_{nN}$. The tensor, $\boldsymbol{\lambda}$, is the symmetric part of the tensor, $\boldsymbol{B}$, and has full Voigt symmetry:

$$\lambda_{ijkl} = \lambda_{jikl} = \lambda_{ijlk} = \lambda_{klij}. \tag{3.28}$$

Substituting Eq. (3.25) into the inequality (3.14) yields necessary conditions for a stable internal equilibrium. The first-order term gives

$$t_{km} = \tau_{km}, \tag{3.29}$$

which requires that the applied (Cauchy) stresses be equal to the thermodynamic stresses that are obtained by differentiating the free energy density with the current configuration as reference state. The second-order term provides the necessary conditions of internal stability. These are embedded in the quadratic form

$$\lambda_{ijkl}\delta\epsilon_{ij}\delta\epsilon_{kl} \geq 0, \tag{3.30}$$

which must be non-negative for arbitrary values of the incremental strains. Since the λ_{ijkl} have Voigt symmetry the stresses, strains and moduli can be written in the usual Voigt notation. Setting $t_{11} = t_1$, $t_{22} = t_2$, $t_{33} = t3$, $t_{23} = t_4$, $t_{13} = t_5$, $t_{12} = t_6$, and making the same replacements for $\delta\epsilon_{ij}$ and λ_{ijkl}, the condition of stability is

$$\lambda_{ij}\delta\epsilon_i\delta\epsilon_j \geq 0, \tag{3.31}$$

where

$$\lambda_{ij} = \frac{1}{2}\left[\frac{\partial t_i}{\partial \epsilon_j} + \frac{\partial t_j}{\partial \epsilon_i}\right]_{\epsilon_k} = \lambda_{ji}, \tag{3.32}$$

where the subscript means that all other ϵ_k are to be held constant. Internal stability requires that the 6×6 matrix of moduli, λ_{ij}, be positive semi-definite. The moduli, λ_{ij}, depend on both the stresses ($\tau_i = t_i$) and the elastic moduli, c_{ij}. Since $\boldsymbol{\lambda}$ is a symmetric matrix, it can be brought into diagonal form with eigenvalues, λ_α, and eigenvectors, $\delta\eta_\alpha$, so that

$$\lambda_{ij}\delta\epsilon_i\delta\epsilon_j = \sum_\alpha \lambda_\alpha \delta\eta_\alpha\delta\eta_\alpha \geq 0. \tag{3.33}$$

Since the eigenvectors, $\delta\eta_\alpha$, are orthogonal (or can be made so), stability requires that all of the eigenvalues be positive. Internal stability is necessarily lost when the least eigenvalue ($\lambda_{\min}$) first falls to a negative value; the limit of elastic stability is, therefore, reached when

$$\lambda_{\min} = 0. \tag{3.34}$$

Note, finally, that when the elastic strains are small, the stresses are small compared to the elastic moduli. Then the equations of linear elasticity apply and

$$\lambda_{ij} \cong c_{ij}. \tag{3.35}$$

In the linear elastic limit the conditions of internal stability reduce to the familiar condition that the 6×6 matrix of elastic moduli, c_{ij}, have no negative eigenvalues.

3.3 Discussion

We began this chapter with a list of three problems: the conditions of stability, stability when some of the loads are controlled, and the proper computation of the limiting strength. We are now in a position to discuss each of them. We shall also discuss three specific cases of particular interest: the cubic solid under hydrostatic pressure, the tetragonal solid under tension along $\langle 100 \rangle$, and the monoclinic solid under shear in $\langle 112 \rangle \{111\}$.

3.3.1 The conditions of stability

The necessary conditions for internal stability are contained in Eq. (3.31) and are given succinctly in Eq. (3.34). These conditions govern internal stability and are, therefore, independent of the nature or behavior of the loading mechanisms. However, Eq. (3.31) is derived from Eq. (3.11), which is the form Eq. (3.1) takes when the loading mechanism fixes the Cauchy stress. It follows that the conditions of internal stability are identical to the conditions of mechanical stability that pertain when the Cauchy stress is controlled [59]. If the loading mechanism that is actually used or supposed in a particular case fixes a set of stresses other than the Cauchy stress, it may impose additional conditions of stability, which may be more stringent than those presented here (see, for example, Hill's discussion of rotational instabilities under dead loading [56]). Still, the conditions of internal stability always apply and are, in this sense, the fundamental conditions. It is appropriate to use them to define the ultimate strength, since the strength cannot exceed the values they allow.

The conditions of stability (3.31) differ from those used in recent work [39, 65] in that only the symmetric part, $\boldsymbol{\lambda}$, of the Wallace tensor, $\boldsymbol{B}$, appears. This happens because the asymmetric part of $\boldsymbol{B}$ does no work in an infinitesimal deformation from the reference state (Wang *et al.* [59] recognize this but use the asymmetric tensor to set the conditions of stability, for reasons that are unclear to the present authors). The difference is small in the cases we have examined.

The identity of the internal conditions of stability with those based on the Cauchy stress shows that the same conditions pertain when the boundary conditions fix the displacement, the Cauchy stress or any combination of displacements and stresses on different parts of the boundary. Many of the most important practical cases fall in the mixed regime. The simplest are uniaxial tension, in which the material is stretched along a particular axis, and simple shear, in which the material is sheared on a particular plane under conditions that are otherwise relaxed.

When the loading mechanism fixes a stress other than the Cauchy stress the internal conditions derived here remain necessary, but may no longer be sufficient to guarantee elastic stability. The second-order response of the loading mechanism may lead to instability before the internal limits are reached. A simple example is a sample under a fixed, uniaxial compressive load; its configuration is unstable with respect to rotations off the axis. Hill [56] poses the problem and treats the conditions of stability under dead loading in some detail. A comprehensive investigation of this issue is needed, but is beyond the scope of the present chapter.

3.3.2 Loading in tension and shear

The simplest cases to picture or analyze are those in which we increment a single strain, ϵ_α, while fixing the other five ϵ_β ("unrelaxed uniaxial strain") or relaxing the stresses, t_β, conjugate to the five ϵ_β ("relaxed uniaxial strain" or "uniaxial stress"). In each of these cases there is only one effective elastic modulus. In the unrelaxed case this modulus is

$$\lambda_{\alpha\alpha} = \left[\frac{\partial t_\alpha}{\partial \epsilon_\alpha}\right]_{\epsilon_\beta} \geq 0, \tag{3.36}$$

while in the relaxed case it is

$$\beta_{\alpha\alpha} = \frac{1}{s_{\alpha\alpha}} = \left[\frac{\partial t_\alpha}{\partial \epsilon_\alpha}\right]_{t_\beta} = \frac{|\boldsymbol{\lambda}|}{\boldsymbol{\lambda}^{\alpha\alpha}} \geq 0, \tag{3.37}$$

where Greek letters label indices that are not summed if repeated. The relaxed modulus, $\beta_{\alpha\alpha}$, is the reciprocal of the compliance, $s_{\alpha\alpha}$, the $\alpha\alpha$ component of the tensor, $\boldsymbol{s}$, that is inverse to $\boldsymbol{\lambda}$ and governs the change of the infinitesimal strains with the Cauchy stresses. It is, therefore, equal to $|\boldsymbol{\lambda}|/\boldsymbol{\lambda}^{\alpha\alpha}$, the determinant of $\boldsymbol{\lambda}$ divided by the cofactor of $\lambda_{\alpha\alpha}$. By LeChatelier's Principle [66], for changes emanating from any given state,

$$\lambda_{\alpha\alpha} \geq \beta_{\alpha\alpha}, \tag{3.38}$$

so the relaxed deformation sets the more stringent limit and leads to a lower ultimate strength. (The equality holds for an isotropic material, as is confirmed by direct calculation for W, which is nearly so. See Chapter 4.) It follows from the final form of Eq. (3.37) that a zero of $\beta_{\alpha\alpha}$ always corresponds to a zero of the determinant $|\boldsymbol{\lambda}|$, and, hence, to a zero of one of its eigenvalues. Relaxed strain does not add any new condition of stability. However, it is well known that the use of Eq. (3.37) can overestimate the limit of strength since other instabilities may intrude prior to its first zero [55]. These instabilities are necessarily associated with simultaneous eigenvalues of $\boldsymbol{\lambda}$ and $\boldsymbol{\lambda}^{\alpha\alpha}$ that divide out on the right-hand side of (3.37). Any such eigenvalue must be associated with an eigenvector that is orthogonal to ϵ_α. As we shall see below, in the cases of interest there are eigenvectors that are orthogonal to the direction of load, ϵ_α,

by symmetry, while others are accidental, and due to the specific values of the λ_{ij} in a particular state. A well-known physical example of the intrusion of an instability is the deformation or failure in shear of a sample pulled in uniaxial tension. Similar instabilities have been seen in simulated cases of deformation under uniaxial loading [39, 58, 67, 68].

3.3.3 Instability in compression, tension or shear

The deformation modes that are most commonly studied are hydrostatic compression, uniaxial tension, and simple shear of initially cubic solids. It is useful to take a moment to summarize the results for these cases.

Hydrostatic compression

Cubic crystals under hydrostatic compression (or tension) were studied in some detail by Wang *et al.* [58, 59]. The crystal retains cubic symmetry, so the λ_{ij} have only three independent values:

$$\begin{aligned} \lambda_{11} &= \lambda_{22} = \lambda_{33} = c_{11} - P \\ \lambda_{12} &= \lambda_{13} = \lambda_{23} = c_{12} + P \\ \lambda_{44} &= \lambda_{55} = \lambda_{66} = c_{44} - P \end{aligned} \tag{3.39}$$

with all other $\lambda_{ij} = 0$. The determinant

$$|\lambda| = {\lambda_{44}}^3(\lambda_{11} - \lambda_{12})^2(\lambda_{11} + 2\,\lambda_{12}) \tag{3.40}$$

is easily factored, yielding three independent conditions of stability:

$$\begin{aligned} c_{44} - P &\geq 0 \\ c_{11} - c_{12} - 2\,P &\geq 0 \\ c_{11} + 2\,c_{12} + P &\geq 0. \end{aligned} \tag{3.41}$$

The third condition relates to the bulk modulus. The first two concern the shear moduli and reveal a tendency toward instability in shear when a material is compressed. Note that in the fluid limit, $c_{44} \to 0$, $c_{11} - c_{12} \to 0$, and the material is unstable in shear when it is compressed but is stabilized by a hydrostatic tension. The "tensile strength" of a fluid in tension is due to Van der Waals' spinodal instability when the bulk modulus is no longer sufficient to support the tensile pressure.

Tetragonal extension

Let an initially cubic crystal be stretched to instability along [100], a situation of obvious interest that has been studied by a number of investigators [37, 39, 41, 55, 68]. The crystal becomes tetragonal as soon as a tensile strain is applied

with the consequence that the modulus tensor ($\boldsymbol{\lambda}$ or $\boldsymbol{c}$) takes the form shown in Eq. (3.42), with five independent components:

$$\boldsymbol{\lambda} = \begin{bmatrix} \lambda_{11} & \lambda_{12} & \lambda_{12} & 0 & 0 & 0 \\ \lambda_{12} & \lambda_{22} & \lambda_{23} & 0 & 0 & 0 \\ \lambda_{12} & \lambda_{23} & \lambda_{22} & 0 & 0 & 0 \\ 0 & 0 & 0 & \lambda_{44} & 0 & 0 \\ 0 & 0 & 0 & 0 & \lambda_{55} & 0 \\ 0 & 0 & 0 & 0 & 0 & \lambda_{55} \end{bmatrix}. \tag{3.42}$$

The applied stress, σ, affects only the components of $\boldsymbol{\lambda}$ that involve the [100] axis:

$$\begin{aligned} \lambda_{11} &= c_{11} + \sigma \\ \lambda_{12} &= c_{12} - \sigma/2 \\ \lambda_{55} &= c_{55} + \sigma/2 \\ \lambda_{ij} &= c_{ij} \qquad \text{(all others).} \end{aligned} \tag{3.43}$$

The determinant of $\boldsymbol{\lambda}$ is given by

$$|\boldsymbol{\lambda}| = (\lambda_{22} - \lambda_{23})\lambda_{44}\lambda_{55}{}^2 \left[\lambda_{11}(\lambda_{22} + \lambda_{23}) - 2\,\lambda_{12}{}^2\right]. \tag{3.44}$$

Its zeros determine four conditions of stability; two of which explicitly involve the applied stress:

$$\lambda_{11}(\lambda_{22} + \lambda_{23}) \geq 2\,\lambda_{12}{}^2 \quad \Rightarrow \quad (c_{11} + \sigma)(c_{22} + c_{33}) \geq 2(c_{12} - \sigma/2)^2 \tag{3.45}$$

$$\lambda_{22} \geq \lambda_{23} \quad \Rightarrow \quad c_{22} \geq c_{23} \tag{3.46}$$

$$\lambda_{44} \geq 0 \quad \Rightarrow \quad c_{44} \geq 0 \tag{3.47}$$

$$\lambda_{55} \geq 0 \quad \Rightarrow \quad c_{55} \geq -\sigma/2. \tag{3.48}$$

Eq. (3.45) differs slightly from the forms presented by Wang *et al.* [59] and by Li and Wang [39]. The difference is due to the symmetry of $\boldsymbol{\lambda}$, which makes a correction of order (σ/c_{12}) to the right-hand side, slightly delaying instability. This term is, ordinarily, small. The modulus that governs a fully relaxed stretch along [100] is

$$\beta_{11} = (s_{11})^{-1} = \frac{\lambda_{11}(\lambda_{22} + \lambda_{23}) - 2\,\lambda_{12}{}^2}{\lambda_{22} + \lambda_{23}}, \tag{3.49}$$

where $\beta_{11} \geq \lambda_{11}$, for an unrelaxed stretch in the same direction. The crystal is unstable with respect to a relaxed stretch on [100] when the condition (3.45) is violated. Since the stretch is tensile, the elastic instability can be accommodated by cleavage on (100). Because a relaxed stretch in any $\langle 100 \rangle$ direction in a bcc crystal produces the fcc structure after a strain of about 0.26 (the Bain strain), the strain of instability will also be approximately 0.13 or less. This $\langle 100 \rangle$ stretch instability strain is significantly smaller than the instability strain for shear in a $\langle 11 \rangle$ direction ($\sim$ 0.18) (see Chapter 4) and is much smaller than

the instability strains for stretches along $\langle 111 \rangle$ or $\langle 110 \rangle$ [68]. This fact that bcc crystals necessarily become unstable after a relatively small stretch along $\langle 100 \rangle$ is presumably responsible for their tendency to cleave on $\{100\}$.

The conditions (3.46)–(3.48) relate to shear strains whose eigenvectors are orthogonal to ϵ_1 by symmetry. The shear instabilities do not produce zeros of β_{11} and may intrude prior to elastic failure by stretch. Shear instabilities of the type (3.46) have been found to intrude in model studies of fcc crystals prior to the zero of β_{11} [68] and appear to be the characteristic strength-determining feature for fcc materials stretched on $\langle 100 \rangle$. This is expected on physical grounds; fcc crystals stretched in tension on $\langle 100 \rangle$ usually fail in shear, via slip on $\{111\}$.

Simple shear

Let an initially cubic crystal be sheared in one of the common slip systems: $\langle 112 \rangle \{111\}$ in fcc, or $\langle 111 \rangle \{110\}$, $\langle 111 \rangle \{112\}$ or $\langle 111 \rangle \{123\}$ in bcc. In each of these cases we can refer the cubic crystal to an orthorhombic cell whose edges parallel the slip direction (for example, $[11\bar{2}]$ in fcc), the normal to the slip plane ($[111]$ in fcc) and a direction perpendicular to both ($[1\bar{1}0]$ in fcc). Shear on the slip plane in the slip direction distorts this cell into one with monoclinic symmetry. If ϵ_6 is taken to be the shear in the slip plane, the tensor moduli then take the form (3.50), with 13 independent terms:

$$\boldsymbol{\lambda} = \begin{bmatrix} \lambda_{11} & \lambda_{12} & \lambda_{13} & 0 & 0 & \lambda_{16} \\ \lambda_{12} & \lambda_{22} & \lambda_{23} & 0 & 0 & \lambda_{26} \\ \lambda_{13} & \lambda_{23} & \lambda_{33} & 0 & 0 & \lambda_{36} \\ 0 & 0 & 0 & \lambda_{44} & \lambda_{45} & 0 \\ 0 & 0 & 0 & \lambda_{45} & \lambda_{55} & 0 \\ \lambda_{16} & \lambda_{26} & \lambda_{36} & 0 & 0 & \lambda_{66} \end{bmatrix}. \tag{3.50}$$

Only four of these include the shear stress:

$$\begin{aligned} \lambda_{16} &= c_{16} + \sigma/2 \\ \lambda_{26} &= c_{26} + \sigma/2 \\ \lambda_{36} &= c_{36} - \sigma/2 \\ \lambda_{45} &= c_{45} + \sigma/2 \\ \lambda_{ij} &= c_{ij} \qquad \text{(all others)}. \end{aligned} \tag{3.51}$$

The determinant of $\boldsymbol{\lambda}$ can be written

$$|\boldsymbol{\lambda}| = \left(\lambda_{44}\lambda_{55} - \lambda_{45}{}^2\right) |\boldsymbol{\lambda_4}|, \tag{3.52}$$

where $\boldsymbol{\lambda_4}$ is the 4×4 matrix obtained from (3.50) by removing the elements associated with ϵ_4 and ϵ_5. $\boldsymbol{\lambda_4}$ contains the maximum possible number of independent elements (10) and cannot be factored in any particularly useful way. The modulus for relaxed shear along ϵ_6 is

$$\beta_{66} = (s_{66})^{-1} = |\boldsymbol{\lambda_4}||\boldsymbol{\lambda_3}|, \tag{3.53}$$

where $\boldsymbol{\lambda_3}(=\boldsymbol{c_3})$ is the 3×3 matrix of terms associated with ϵ_1, ϵ_2 and ϵ_3. β_{66} is independent of the factor $[\lambda_{44}\lambda_{55} - {\lambda_{45}}^2]$, which governs stability with respect to shear in two perpendicular planes. However, since neither $|\lambda_4|$ nor $|\lambda_3|$ can be factored, any other instability prior to the zero of β_{66} would be fortuitous. Instabilities along ϵ_4 and ϵ_5 can be relevant. For example, in Al and in (presumably) most other fcc materials, any finite shear in the $[10\bar{1}]$, direction on the (111) plane is unstable with respect to rotation toward $[11\bar{2}]$ or $[\bar{1}\bar{1}2]$ The relaxations that accomplish this rotation are shears along ϵ_4 and ϵ_5.

3.3.4 *Ab initio* calculations of the elastic limits

Recent advances in theoretical methods and computing machines make it possible to calculate the energies of distorted crystal lattices to very high accuracy. The computations are tedious, however, particularly when the distorted solid has low symmetry. For this reason most first-principles calculations of the elastic limits have studied the behavior of materials with primitive lattices in uniaxial stretch along axes of high symmetry [37, 39], or simple shear in one of the preferred slip systems [31, 32, 40, 41]. Simpler models have been used to clarify the symmetry rules that locate extrema in simple crystal structures under various types of loading (Ref. [68] and references cited therein), or to conduct molecular dynamic studies of the approach to elastic instability [58, 59, 65].

The most straightforward way to calculate elastic limits from first principles is to simply stretch, compress or shear the crystal in the desired direction, compute the elastic energy and the relevant Cauchy stress as a function of strain, and look for the maximum of the stress. In the relaxed case, which is clearly the most informative, the crystal must be reconfigured at every step to relax the lateral stresses. This can be done in a straightforward manner by computing the stresses via the Hellman-Feynman method and reconfiguring the atoms until the lateral stresses relax to zero (see Chapter 2). In the general case, the Cauchy stress is found by computing the energy increment in a small incremental strain. When the total strain is small, however, as it is to a fair approximation in structural metals under simple loading even at the elastic limit (see Chapter 2), linear elasticity applies and the Cauchy stress is given by the slope of a plot of the free energy as a function of strain. In that case elastic instabilities are identified by inflection points in the free energy curve.

This uniaxial procedure has the disadvantage that it yields only an upper bound on the theoretical strength. As discussed above, instabilities along eigenvectors perpendicular to the direction of stretch are not seen, and may intrude at lower values of the stress. The only mathematically rigorous way to ensure that all of these are found is to compute the full set of elastic constants after each strain increment and test for zeros of $|\boldsymbol{\lambda}|$. Practically, however, it is only necessary to apply a set of small triclinic distortions and to allow relaxation from the distorted states. Only if all of these triclinic distortions are fortuitously parallel to the minimal eigenvector of $\boldsymbol{\lambda}$ will any instability be missed. Unfortunately, since a triclinic crystal has no symmetry other than the inversion operation, these computations are still difficult to do.

By combining the uniaxial procedure with a few low symmetry distortions and a bit of physical insight, one can obtain answers that are very likely to be right. If one has computed both the strength in tension along the obvious symmetry axes and the strength in shear in the common slip systems then one can test the probability that slip intrudes prior to tensile failure by computing the resolved shear stress under a tensile load that approaches the theoretical strength. If the shear stress is well below the relevant shear strength, shear instabilities are unlikely. A similar method can test the likelihood that tensile failure intrudes during deformation in shear. If these or other orthogonal instabilities are possible, they will almost certainly pertain over a range of strain prior to instability in uniaxial load. It should ordinarily be sufficient to test the crystal with small triclinic distortions at a few isolated points prior to instability. This is particularly the case in relaxed shear (see Chapter 2) since the reconfigurations that are necessary to relax the stresses sample all deformations but ϵ_4 and ϵ_5.

3.4 Conclusion

The internal conditions of stability are found by applying Gibbs' criterion that the material be stable to all reconfigurations that do not alter its boundary. The conditions of stability are contained in the requirement that $\lambda_{ijkl}\delta\epsilon_{ij}\delta\epsilon_{kl} \geq 0$ for all infinitesimal strains, where $\lambda_{ijkl} = 1/2(B_{ijkl} + B_{klij})$, and $\boldsymbol{B}$ is the tensor that governs the change in the Cauchy stress ($\boldsymbol{t}$) during incremental strain from a stressed state ($\boldsymbol{\tau}$): $t_{ij} = \tau_{ij} + B_{ijkl}\delta\epsilon_{kl}$. Since $\boldsymbol{\lambda}$ has full Voigt symmetry, it can be written as the 6×6 matrix, λ_{ij}, with eigenvalues, λ_α. Stability is lost when the least of these vanishes. The conditions of internal stability are shown to be equivalent to those derived previously for a solid in contact with a reservoir that fixes and maintains the Cauchy stress. Mechanisms that control stresses other than the Cauchy stress may add additional conditions of stability, which may be more stringent, but cannot obviate these. The conditions of stability are exhibited for cubic (hydrostatic), tetragonal (tensile) and monoclinic (shear) distortions of a cubic crystal and some of their implications are discussed. Elastic stability and the limits of strength are now being explored through first-principles calculations that increment uniaxial stretch or shear to find the maximum stress. This method produces an upper bound, but it may not be the least upper bound since orthogonal instabilities may intrude before it is reached. This possibility can often be recognized or dismissed on the basis of a few supplementary calculations.

Chapter 4

The Ideal Strength of Tungsten[†]

4.1 Introduction

4.1.1 Tungsten as an further example

Chapter 2 looked at the ideal shear strengths of the fcc metals Al and Cu. In this chapter, we examine the ideal shear and tensile strengths of bcc tungsten. Tungsten was chosen for three reasons. First, it is a good example of the bcc transition metals, which provide technologically important structural materials. The most important of all, of course, is Fe, but the ferromagnetic interaction in bcc Fe makes it a very difficult subject for fundamental study [69]. Tungsten is a more tractable example.

Second, bcc transition metals like tungsten have complex and interesting mechanical properties [70]. They commonly shear on at least three different crystallographic slip systems, $\langle 111\rangle\{110\}$, $\langle 111\rangle\{112\}$ and $\langle 111\rangle\{123\}$, and sometimes exhibit such a mixture of these (and, possibly, others) that their deformation is described as "pencil glide" on arbitrary planes that contain $\langle 111\rangle$ [71]. Despite this multiplicity of slip systems, bcc crystals are characteristically brittle at low temperature, a behavior that, in the case of Fe, is responsible for a good many of the better-known engineering disasters of the industrial age. It is of interest to know whether these characteristic behaviors of bcc crystals are reflected in their ideal strength.

Third, tungsten was chosen because there has been an *ab initio* study of its tensile behavior [38], which provides a cross-check on the accuracy of the results.

[†]The research presented in this chapter has been submitted for publication (Ref. [33].)

4.1.2 Choice of strain paths

The ideal strengths of all crystalline solids vary with the geometry of the applied strain. For example, the strength of a model fcc crystal stressed in shear on a $\{111\}$ plane in a $\langle 112 \rangle$ direction will always be lower than the strength for shear in a $\langle 110 \rangle$ direction on the same plane. Fortunately, principles of symmetry and exploratory calculations have shown that highly symmetric loading geometries set the upper and lower bounds of strength. Most important are the lower bounds, and it follows that we must calculate separate strengths for shear and tension in only a small number of high-symmetry loading configurations.

We shall specifically consider five simple configurations: uniaxial tension along $\langle 100 \rangle$, shear on the three common slip systems, and shear on the uncommon system $\langle 110 \rangle \{110\}$. We justify these choices on the following grounds, which we shall discuss in further detail in the body of the chapter.

The tensile calculation is done along $\langle 100 \rangle$ because symmetry arguments [72], prior computations [38] and empirical testing [73] all identify the $\langle 100 \rangle$ axes as the weak directions in tension and the $\{100\}$ planes as the cleavage planes. Similarly, experimental data [70] and symmetry considerations (that were found in the course of this work) all identify slip in $\langle 111 \rangle$ directions on $\{110\}$, $\{112\}$ and $\{123\}$ planes as comparable candidate systems for the minimum strength in shear. The $\langle 110 \rangle \{110\}$ system is treated as an example of an unfavorable shear.

We have not specifically treated multiaxial stresses. However, both prior pseudopotential calculations by Söderlind and Moriarty [42] and our own exploratory calculations with "embedded atom" (EAM) methods [74] suggest that, excepting very high hydrostatic pressure, secondary stresses do not have an important effect on the ideal strength.

4.1.3 Definition of the ideal strength

Even when the stress is uniaxial there is some ambiguity in the definition of the ideal strength (see Chapter 3). In a laboratory test, elastic stability is a joint property of the material and the loading mechanism [56, 57]. The maximum value of the measured strength depends on the response of the loading mechanism to second-order displacements [56]. We use the analysis of ideal strength developed in Chapter 3 and define the ideal strength by the limit of internal stability, the stress at which the crystal first becomes unstable with respect to quasi-static distortions that do not displace its boundary. The ideal strength that is measured in this way is equal to that which would be measured in a test with a load frame that fixed the Cauchy stress (force per unit area in the current configuration) to the second order [58].

As derived in Section 3.2, if the current state of the crystal is described by the Lagrangian strain, $\boldsymbol{E}$, and the Cauchy stress, $\boldsymbol{\sigma}$, its internal stability is governed by the fourth-order tensor $\boldsymbol{\lambda}$:

$$\lambda_{ijkl} = c_{ijkl}(\boldsymbol{E}) + \frac{1}{2}(\sigma_{ik}\delta_{jl} + \sigma_{il}\delta_{jk} + \sigma_{jk}\delta_{il} + \sigma_{jl}\delta_{ik} - \sigma_{ij}\delta_{kl} - \sigma_{kl}\delta_{ij}), \quad (4.1)$$

where $\boldsymbol{c}$ is the tensor of elastic moduli at strain, $\boldsymbol{E}$. Stability requires that $\boldsymbol{\lambda}$ (or, more simply, its 6×6 Voigt form) have no non-zero eigenvalues. Since both $\boldsymbol{c}$ and $\boldsymbol{\sigma}$ change with strain and $\boldsymbol{\lambda}$ has six independent eigenvalues, testing stability can be a formidable task.

Fortunately, if the deformation is uniaxial and fully relaxed, the strength defined by the limit of internal stability (the ideal strength) is ordinarily just the maximum value of the conjugate Cauchy stress. This is true unless the solid is unstable to perturbations that are orthogonal to the direction of the applied load. Orthogonal instabilities are unlikely unless the load is along a direction of high symmetry, and can be revealed by periodically perturbing the crystal with distortions that create triclinic symmetry (see Chapter 3). When the deformation is uniaxial and fully relaxed, the elastic limit is not difficult to find in practice.

Unfortunately, even these techniques miss dynamic instabilities, such as those caused by "soft phonons" or anharmonic vibrations. The ideal strengths computed here refer to the limit of internal stability under quasi-static deformation in the low-temperature limit.

In the following we first compute the ideal strength of W in uniaxial tension along $\langle 100 \rangle$ and compare the results to prior work. Second, we compute the ideal strength in shear for the three experimentally observed slip systems, $\langle 111 \rangle \{110\}$, $\langle 111 \rangle \{112\}$ and $\langle 111 \rangle \{123\}$, and for the alternate system $\langle 110 \rangle \{110\}$. The remarkable result of this calculation is the almost identical value of the ideal strength for $\langle 111 \rangle$ slip on the three different slip planes. Third, we discuss the symmetries of the deformations considered. Symmetry considerations let us formulate simple models that approximate the ideal strengths to within a few percent and explain the degeneracy of the strengths in shear along $\langle 111 \rangle$. Finally, we compare the results to experimental values reported from both tensile tests of tungsten whiskers and nanoindentation measurements on tungsten films and discuss the differences.

4.2 Computational Methods

The computational procedure used here was essentially the same as that of Chapter 2. The tungsten unit cell is defined by three lattice vectors, $\boldsymbol{a}^\alpha$ ($\alpha = 1, 2, 3$) and placed in a Cartesian coordinate system with axes $\boldsymbol{e}_i$ ($i = 1, 2, 3$). The lattice vectors $\boldsymbol{a}^1$ and $\boldsymbol{a}^2$ are taken to lie in the plane of $\boldsymbol{e}_1$ and $\boldsymbol{e}_2$. The unit cell is deformed by incremental changes in the lattice vector, $\boldsymbol{a}^3$. To model uniaxial tension along [100], $\boldsymbol{a}^3$ is incremented by $\Delta \boldsymbol{a}^3$ in the direction of $\boldsymbol{e}_3$, which is parallel to [100]. To model shear in the system $[abc](hkl)$ the coordinate vectors $\boldsymbol{e}_1$ and $\boldsymbol{e}_2$ are taken to lie in the plane (hkl) with $\boldsymbol{e}_1$ parallel to the direction $[abc]$. The deformation is accomplished by incrementing $\boldsymbol{a}^3$ by $\Delta \boldsymbol{a}^3$ in the direction of $\boldsymbol{e}_1$.

The deformed lattice vectors, $\boldsymbol{a}^\alpha$, define the current shape of the unit cell and, hence, the current positions of all the atoms. When the deformation is finite, there is no unique way to translate this information into a tensor strain [49].

But there is a unique measure of the stress that governs mechanical stability: the Cauchy (or "true") stress, which is the applied force per unit area in the current configuration of the crystal (Chapter 3). As in Chapter 2 we define strains and estimate the Cauchy stresses as follows:

Let $\boldsymbol{a}^\alpha(0)$ be the α^{th} lattice vector in the unstressed bcc crystal, and let $\boldsymbol{a}^\alpha(n)$ be its vector value after the n^{th} incremental step in the deformation. The net deformation between steps m and n is defined by the tensor $\boldsymbol{D}(n,m)$:

$$a_i^\alpha(n) = a_i^\alpha(m) + D_{ij}(n,m)\, a_j^\alpha(m). \tag{4.2}$$

The incremental strain in the n^{th} step, $\boldsymbol{\Delta\epsilon}(n)$, is, then

$$\Delta\epsilon_{ij}(n) = \frac{1}{2}\left[D_{ij}(n,n-1) + D_{ji}(n,n-1)\right], \tag{4.3}$$

and we can define a "true" strain as

$$\epsilon_{ij}(n) = \sum_{m=1}^{n} \left[\Delta\epsilon_{ij}(m)\right]. \tag{4.4}$$

Since the values of $\epsilon_{ij}(n)$ are sensitive to the number of steps in the simulation, it is useful to define a measure of strain independent of this, the engineering strain:

$$e_{ij} = \frac{1}{2}\left[D_{ij}(n,0) + D_{ji}(n,0)\right]. \tag{4.5}$$

Note that the engineering strain e_{ij} is just the linear part of the Lagrangian strain, E_{ij}:

$$E_{ij} = \frac{1}{2}\left[D_{ij}(n,0) + D_{ji}(n,0) + D_{ki}(n,0)D_{kj}(n,0)\right]. \tag{4.6}$$

The Cauchy stress $\boldsymbol{\sigma}$ in the n^{th} step can be estimated in three ways. First, the stresses can be found from the change of the total energy U with the conjugate incremental strains:

$$\sigma_{ij}(n) = \frac{1}{V(n)}\left[\frac{\Delta U(n)}{\Delta\epsilon_{ij}(n)}\right], \tag{4.7}$$

where $V(n)$ is the current volume of the crystal. However, this definition is very sensitive to small errors in U and $\boldsymbol{a}^\alpha$. Since, in most cases, U and $\boldsymbol{a}^\alpha$ vary smoothly and continuously with strain, differentiating a smoothed fit through a plot of U versus "true" strain reduces errors in stress at each point:

$$\sigma_{ij} = \frac{1}{V}\left[\frac{\partial U}{\partial\epsilon_{ij}}\right]. \tag{4.8}$$

In the limit of small $\Delta\epsilon$ (large number of steps for a finite strain), this will converge to the thermodynamic definition of the Cauchy stress. Equation (4.8)

offers the most precise estimate of stress from the available data, but we do note that, in the cases studied here, the strains are small enough that the stresses are also well approximated by the derivative of the energy with respect to the engineering strain. The third way to determine the stresses is from the Hellman-Feynman theorem [75, 76]. The directly calculated stresses have less precision than the energy, because the energy is calculated variationally. However, they have the advantage that they are independently calculated for each strain, and thus provide a check that our strain increments are sufficiently small.

In the present work, the quasi-static (T=0) energy of the deformed crystal and the Hellman-Feynman stresses were calculated using the local density approximation (LDA) within a pseudopotential total-energy scheme incorporating semi-relativistic corrections [36, 43–47]. Using a cut-off energy of 60 Ry with a $16 \times 16 \times 16$ k point grid generated using the Monkhorst-Pack scheme proved sufficient to achieve precision of better than 1 mRy (0.013 eV) in the calculated energies.

The energy and stress were calculated as a function of strain for both uniaxial strain (unrelaxed condition) and uniaxial stress (relaxed condition). In the former case, a selected strain was incremented while the other five independent strains were fixed at zero. In the latter case, which provides a more meaningful measure of the ideal strength, the crystal was relaxed until only the stress, t_{ij}, conjugate to the selected strain had a non-zero value. This was done by fixing the selected strain and adjusting the other five independent strains until their conjugate Hellman-Feynman stresses were less than 0.15 GPa.

4.3 Ideal Strength

4.3.1 The lattice constant and elastic moduli

A first test of the accuracy of the computational scheme is its ability to predict the lattice constant and the elastic moduli of the crystal. The results are shown in Table 4.1, which includes the lattice parameter and bulk modulus, and the elastic modulus and compliance for shear in the system $\langle 111 \rangle \{110\}$. The lattice parameter is accurate to within 1%, the moduli are correct to within 6%. Since W is almost isotropic at 0 K (the anisotropy ratio $(c_{11} - c_{12} - 2\,c_{44})/c_{44}$, where c_{ij} are the Voigt elastic constants, is less than 0.01 [77]), the shear modulus, $c_{\langle abc \rangle \{hkl\}}$, and the elastic compliance, $s_{\langle abc \rangle \{hkl\}}$, for shear on any slip system, $\langle abc \rangle \{hkl\}$ are given by

$$G_{\langle abc \rangle \{hkl\}} \approx \frac{1}{s_{\langle abc \rangle \{hkl\}}} \approx c_{44}. \tag{4.9}$$

Because tungsten is elastically isotropic, the combination of the bulk and shear moduli are sufficient to fully specify its elastic properties.

However, as in the discussion in Section 2.3 on the lattice constant of Al, it is somewhat troubling that our computed lattice constant using LDA is larger than the experimental value. It is also unusual that both the lattice constant

Table 4.1: Calculated (LDA) and experimental lattice parameters and elastic moduli of bcc tungsten.

	experimental	present work	PP[c]	FP-LMTO[c]
lattice constant (Å)[a]	3.16	3.17	3.13	3.15
$c_{\langle 111\rangle\{110\}}$ (GPa)[b]	164	161 ± 1	–	–
$1/s_{\langle 111\rangle\{110\}}$ (GPa)[b]	164	159 ± 1	–	–
bulk modulus (GPa)[b]	314	331 ± 1	317	319

[a]Experimental values at 298 K are from Ref. [11].
[b]Experimental 4.2 K data are from Ref. [77].
[c]Values are from an *ab initio* study of tungsten in Ref. [78] and are computed using both pseudopotential plane wave (PP) and full-potential, linear muffin-tin-orbital (FP-LMTO) techniques.

and the bulk modulus are larger than experiment. Table 4.1 includes results from another recent *ab initio* study of tungsten using both pseudopotential plane wave (PP) and full-potential, linear muffin-tin-orbital (FP-LMTO) techniques. Because the lattice constants predicted by these calculations are smaller than experiment, these results are more believable than our own. As argued in Section 2.3, however, any small errors in the pseudopotential will not have a large effect on either our computed values of ideal strength or on our analysis of the structural relaxations of tungsten under load.

4.3.2 The ideal strength in tension

Figure 4.1 shows the variation of energy (Fig. 4.1a) and stress (Fig. 4.1b) with engineering strain for a crystal that is pulled in a $\langle 100\rangle$ direction with full relaxation along the perpendicular axes. The maximum tensile stress, σ_m, is 29.5 GPa, in close agreement with the value, 28.9 GPa, reported by Šob *et al.* [38]. Šob *et al.* also calculated tensile strengths in the $\langle 111\rangle$ and $\langle 110\rangle$ directions. These are substantially higher.

The reason that bcc crystals are weak in $\langle 100\rangle$ directions (and, therefore, cleave on $\{100\}$ planes) has been known for some time [79]. As illustrated in Fig. 4.2, if a bcc crystal is pulled along $\langle 100\rangle$ and allowed to relax in the two perpendicular directions its structure eventually becomes fcc. Assuming constant volume, the engineering strain, e_3, needed to accomplish the transformation (the "Bain strain") is $e_b = 0.26$. Since the stress vanishes by symmetry in both the bcc and fcc structures, either the fcc structure must be a saddle point, or it must pass through a maximum at some intermediate strain. No similar extrema are fixed by symmetry for the other possible directions of tensile loading. Hence, barring accidental extrema, a bcc crystal has its minimum tensile strength when it is loaded on $\langle 100\rangle$.

The ideal tensile strength can be estimated in the following way (which is generally applicable to any bcc crystal whose energy increases monotonically

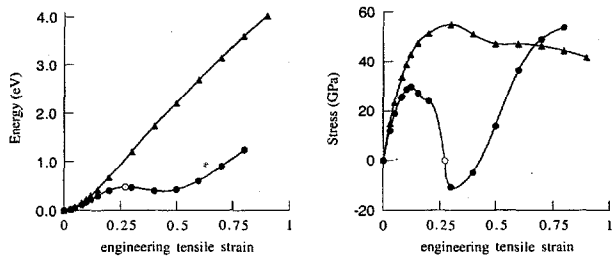

a) b)

Figure 4.1: Energy (a) and stress (b) as a function of applied tensile strain applied along ⟨100⟩ to bcc tungsten. The ▲'s are for the unrelaxed cases and the ●'s for the relaxed cases. The ⊙'s mark the position of fcc tungsten.

when it is stretched from bcc to fcc along ⟨100⟩). In the tradition of Frenkel [80] and Orowan [81] we approximate the stress-strain curve by a sinusoidal function with a period of e_b. In this case,

$$\sigma = \sigma_m \sin\left[\frac{\pi e}{e_b}\right], \tag{4.10}$$

where σ_m is the maximum stress. Since $\sigma = E_{\langle 100\rangle} e$, when e is small (Hooke's Law) and $E_{\langle 100\rangle}$ is Young's modulus for a ⟨100⟩ stretch,

$$\sigma_m = \left[\frac{e_b}{\pi}\right] E_{\langle 100\rangle} = 0.08\, E_{\langle 100\rangle}. \tag{4.11}$$

The *ab initio* calculation for W gives 29.5 GPa, which is $0.072\, E_{\langle 100\rangle}$, in reasonably good agreement.

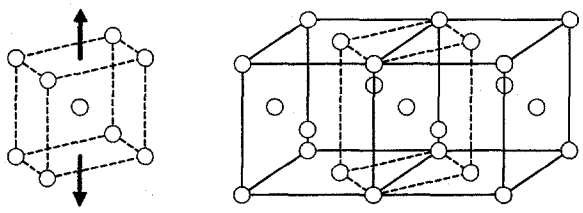

Figure 4.2: Illustration of the Bain transformation path between bcc and fcc.

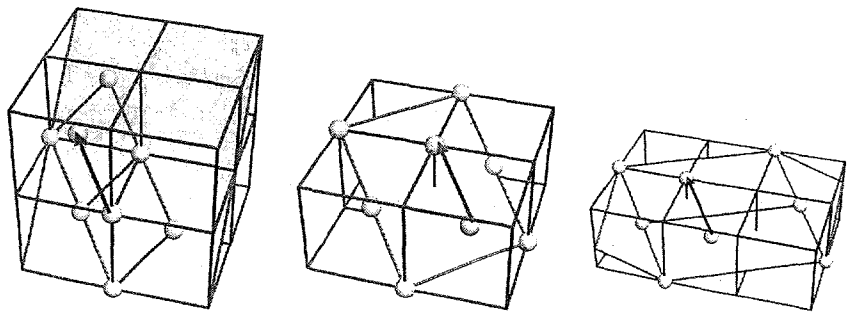

Figure 4.3: Geometries of shear for slip on {110}, {112}, and {123} planes along a ⟨111⟩ direction. The atoms connected by the arrows are sheared over the plane below. The arrowheads indicate the "easy" direction of shear.

4.3.3 The ideal strength in shear

The common bcc slip systems, ⟨111⟩{110}, ⟨111⟩{112} and ⟨111⟩{123}, are illustrated in Fig. 4.3. The ⟨111⟩{110} system is symmetric with respect to the direction of shear along the ⟨111⟩ axis. The ⟨111⟩{112} and ⟨111⟩{123} systems are not; slip in the direction of the arrow shown in the figure (the "easy" direction) has a lower shear strength and energetic maximum than slip in the opposite direction (the "hard" direction).

Fig. 4.4 includes plots of energy against engineering strain for the three slip systems over a full period of shear along ⟨111⟩. The strain periods for the relaxed and unrelaxed shears differ because the former includes relaxations orthogonal to the applied shear. Fig. 4.5 is the engineering stress-strain relation for slip on the ⟨111⟩{112} system. This figure also shows the agreement between the calculated Hellman-Feynman stresses and the Cauchy stress estimated from the slope of the energy-strain curve. Fig. 4.6 presents the most striking result of these calculations: the close similarity of the stress-strain relations for ⟨111⟩ slip in the easy directions on the three planes.

Table 4.2 lists the shear strengths for the three slip systems in relaxed and unrelaxed strain in both the "easy" and "hard" directions. Table 4.3 lists the strains at each instability (the shear strain $\gamma_{ij} = 2e_{ij}$). Tables 4.2 and 4.3 also include data for the ⟨110⟩{110} system. As it is to be expected, the relaxed strengths are lower than the unrelaxed in all cases, and the strengths in "easy" slip are much below those in the "hard" directions. The relaxed strength in the (symmetric) ⟨110⟩{110} system ($\approx 0.12\,G$) is higher than that for "easy" slip in any of the ⟨111⟩ systems studied ($\approx 0.11\,G$ for all three systems).

The shear of W in the ⟨111⟩{112} system was previously studied by Paxton *et al.* [40] for unrelaxed and partially relaxed shears. They obtained a strength

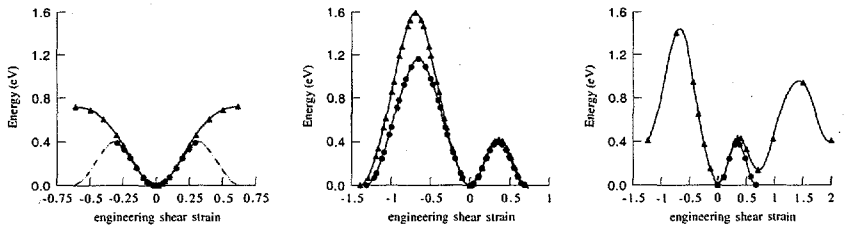

Figure 4.4: Energy as a function of applied shear strain for one period of ⟨111⟩ slip on {110}, {112}, and {123} planes. The ▲'s are for the unrelaxed cases and the ●'s for the relaxed cases.

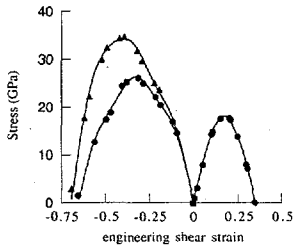

Figure 4.5: Absolute values of the stress as a function of strain for ⟨111⟩{112} slip. The ▲'s and the ●'s are the calculated unrelaxed and relaxed Hellman-Feynman stresses. The solid lines represent the stresses calculated from smoothed fits to the energies.

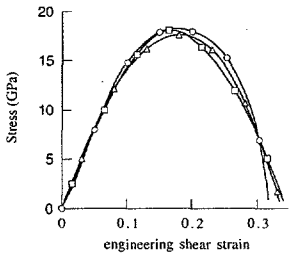

Figure 4.6: Fitted stresses as a function of strain for ⟨111⟩ slip in the "easy" direction on {110} (○'s), {112} (□'s), and {123} planes (△'s).

Table 4.2: Ideal shear strengths ($\tau_{\max}$) with (r) and without (u) structural relaxations for five slip systems. G is the experimental shear modulus.

	failure stresses (GPa and %)			
slip system	$\tau^r_{\max}$	$\tau^u_{\max}$	$\tau^r_{\max}/G$	$\tau^u_{\max}/G$
$\langle 111\rangle\{110\}$	18.2 ± 0.4	20.8 ± 0.4	11.2	12.7
$\langle 110\rangle\{110\}$	19.3 ± 0.4	21.3 ± 0.4	11.8	13.0
$\langle 111\rangle\{112\}_{\text{easy}}$	18.1 ± 0.4	19.2 ± 0.4	11.1	11.7
$\langle 111\rangle\{112\}_{\text{hard}}$	26.3 ± 0.8	34.3 ± 0.8	16.1	21.0
$\langle 111\rangle\{123\}_{\text{easy}}$	17.6 ± 0.8	19.1 ± 0.8	10.8	11.7
$\langle 111\rangle\{123\}_{\text{hard}}$	>20	30.6 ± 0.8	>12	18.7

of $0.13\,G$ for unrelaxed shear in the "easy" direction and $0.27\,G$ in the "hard" direction. These values are somewhat higher than ours (Table 4.2), but may result from additional approximations used in their total-energy calculations.

Compared to the results for Al and Cu, in which relaxation decreased ideal strengths by 35% to 45%, relaxation has a relatively small effect on the strength of W. This is primarily due to the elastic isotropy of W, which has the consequence that the second-order shear moduli are the same for relaxed and unrelaxed strain. The two cases differ only to the extent that third- and higher-order moduli influence the results. Relaxation does have a significant effect ($> 20\%$) on the strength of the $\langle 111\rangle\{112\}$ system in the "hard" (negative) direction. Table 4.3 shows that this results from large values of the relaxation strain. These large relaxation strains have two sources. First, the primary shear strain at instability is large (≈ -0.33), so non-linear effects make significant contributions. Second, as illustrated in Fig. 4.7, in a relaxed shear the lattice becomes unstable and deforms discontinuously at a shear of -0.45. While this structural instability lies beyond the elastic instability at the maximum shear stress, its proximity will soften the lattice, decreasing its strength.

Table 4.3: Applied (γ_{13}) and relaxation engineering strains at shear instability.

		relaxation strains (%)					
instability	γ_{13}	ϵ_{11}	ϵ_{22}	ϵ_{33}	γ_{12}	γ_{23}	$\Delta V/V$
$\langle 111\rangle\{110\}$	17.4	-1.2	0.1	2.5	0.5	-0.8	1.4
$\langle 110\rangle\{110\}$	15.8	-0.3	-0.8	2.1	0	0	0.9
$\langle 111\rangle\{112\}_{\text{easy}}$	16.8	-1.0	0.6	1.5	0	0	1.1
$\langle 111\rangle\{112\}_{\text{hard}}$	32.7	-2.8	2.3	4.9	0	0	4.4
$\langle 111\rangle\{123\}_{\text{easy}}$	18.2	-1.2	0.5	2.0	-0.8	0.0	1.3

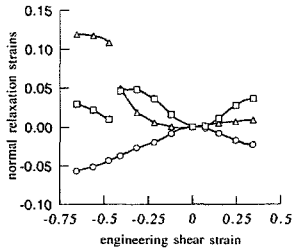

Figure 4.7: Normal relaxation strains as a function of applied shear strain for $\langle 111\rangle\{112\}$ slip. (○'s: ϵ_{11}, □'s: ϵ_{22}, and △'s: ϵ_{33}) A structural shear instability is clearly visible at a strain of approximately -0.45.

4.3.4 Sources of the ideal strength in shear

The best single measure of the ideal shear strength is the minimum value of the relaxed strength for the "easy" direction of slip. This strength sets the maximum yield stress of an otherwise ideal polycrystal. Even a single crystal loaded for slip in the "hard" direction on $\{112\}$ would exceed the critical stress for slip on $\{110\}$ before reaching the "hard" strength on $\{112\}$. From this perspective, the present calculations give the ideal shear strength of W as 17.6 GPa ($.108\,G$) for shear in the system $\langle 111\rangle\{123\}$. Because the shear strengths on $\langle 111\rangle\{110\}$ and $\langle 111\rangle\{112\}$ are so close to this value, a more exact calculation of an ideal yield surface would find the shear strength to be practically isotropic.

Not only are the ideal strengths in the three common slip systems almost identical ($\approx$ 18 GPa $= 0.11\,G$), but the failure strains are almost the same as well, 17–18%. This contradicts the usual assumption that the ideal strength is proportional to (b/h), where h is the interplanar spacing and b, the Burger's vector, is the length of the shortest lattice vector in the direction of slip. The shear strength on the $\{110\}$ planes, which are the closest-packed and most widely spaced, is essentially the same (in fact, it is a bit higher) than that on $\{123\}$ planes that are much closer together. The insensitivity to (b/h) is due to the fact that, for all three planes studied, the elastic instability (the first inflection point on the energy curve) falls at only a small fraction of the minimal crystallographic translation in the $\langle 111\rangle$ direction.

The shortened period for slip in the $\{112\}$ plane has been noted before [40, 82], and can be understood from an inspection of the atom configuration in the $\{112\}$ plane (Fig. 4.8). A shear strain of 0.66 in the easy direction is the "twinning strain" that creates a mirrored bcc lattice. It follows that there must be at least one maximum in the energy at a strain below 0.66, and an elastic instability (inflection point) before that. If there is a single maximum, symmetry dictates that it falls at $\gamma = 0.33$, with an inflection near 0.167, which is almost exactly the strain ($\gamma = 0.168$) that the *ab initio* calculation finds for elastic instability in shear on $\{112\}$.

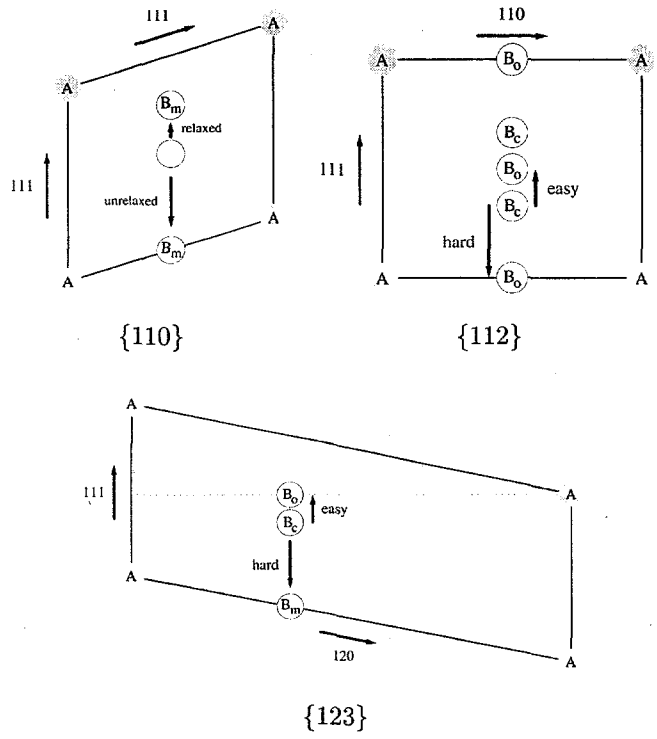

Figure 4.8: Illustrations of the changes in symmetry during relaxed shear on {110}, {112}, and {123} planes. A and B atoms are on two adjacent planes. A B_c position indicates a lattice with cubic symmetry, a B_m position monoclinic symmetry, and a B_o position orthorhombic symmetry. Intermediate configurations during shear on the {110} and {123} planes have triclinic symmetry. The intermediate configurations during shear on {112} have monoclinic symmetry.

While the symmetry constraints that govern the shear instability on {112} may be obvious, the triple period on {123} was not apparent until the energy had been calculated. The shear instability on {110} was also invisible until the fully relaxed case had been explored. A closer examination shows that the extrema that locate the first instability on each of these paths are associated with local configurations of relatively high symmetry. Figure 4.8 illustrates this. A ⟨111⟩{110} shear changes the symmetry from cubic to triclinic; the first extremum occurs when the deformed path passes through a configuration with monoclinic symmetry. In the ⟨111⟩{112} system, the shear deformation path moves from cubic to monoclinic to orthorhombic symmetry at the first extremum. In the ⟨111⟩{123} system, the sequence is cubic to triclinic to orthorhombic.

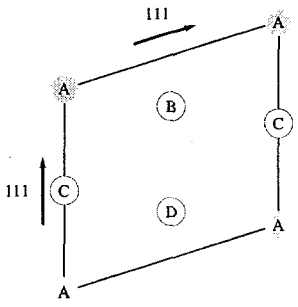

Figure 4.9: Illustration of the stacking sequence for the saddle point of ⟨111⟩-{110} slip (ABCDA).

Although the energies and strains at the first extrema on the three slip systems are almost identical, the extremal structures are not. The extremal structure on {110} has a monoclinic Bravais lattice with three atoms per unit cell and $ABCDA$ stacking as shown in Fig. 4.9. The extremal structure along {112} is a body-centered orthorhombic lattice formed by the $AB_0^{\text{easy}}A$ stacking shown in Fig. 4.8. This, as we shall show below, is also the extremal structure on {123}.

The similar strengths and instability strains on the three common bcc slip systems has a straightforward geometrical explanation. If we locate a bcc atom at the center of the bcc cell then, as illustrated in Figs. 4.10 and 4.11a, two of its nearest neighbors lie along the cube diagonal while the other twelve nearest and next-nearest neighbors sit at the corners of two pairs of equilateral triangles that are perpendicular to the cube diagonal. A shear in the ⟨111⟩ direction tilts each of these triangles along the ⟨111⟩ axis around an axis in the shear plane. The

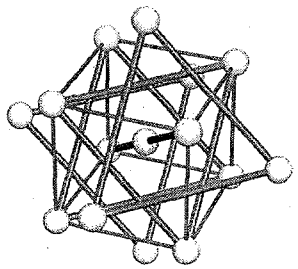

Figure 4.10: Illustration of the stacking sequence of the eight nearest and six next-nearest neighbors along the ⟨111⟩ direction in bcc.

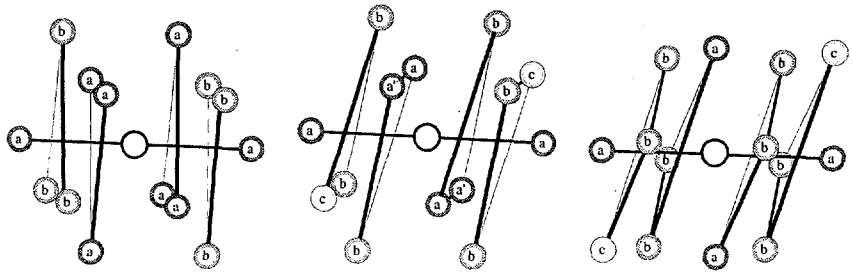

a = 5.2Å
b = 6.0Å

a = 5.1Å
a' = 5.3Å
b = 5.7Å
c = 7.0Å

a = 5.1Å
b = 5.6Å
c = 7.2Å

a) b) c)

Figure 4.11: Illustration of the symmetries of pencil glide in bcc. The tables list the distance of each labeled neighboring atom from the central atom. a) shows an unstrained tungsten bcc lattice, b) shows the saddle point after $\langle 111 \rangle \{110\}$ shear, and c) shows the symmetry of the $\{112\}$ and $\{123\}$ saddle point.

cubic symmetry is broken, and the set of eight nearest neighbors and six next-nearest neighbors is replaced by seven pairs of near-neighbor atoms at varying distances. As the triangles tilt in the $\langle 111 \rangle$ direction and relax around the $\langle 111 \rangle$ axis, their corners approach one another. The energy extrema are reached when the corners of the coordination triangles first come into partial registry with one another, as illustrated in Fig. 4.11b (the $\{110\}$ extremum) and Fig. 4.11c (the $\{112\}$ and $\{123\}$ extremum).

The spatial registry of the coordination triangles at the extremum changes the number of equidistant neighbors and creates a more symmetric configuration. As illustrated in Fig. 4.11b, the $\{110\}$ extremum has 6 neighbors at distances of 5.1–5.3Å and 6 neighbors at 5.7Å. The extremal configuration for $\{112\}$ and $\{123\}$ slip is the same (Fig. 4.11c). It has four neighbors at a distance of 5.1Å and eight at 5.6Å. As shown in Figs. 4.8 and 4.9, these symmetric arrangements have monoclinic and orthorhombic Bravais lattices, respectively. The extrema on $\{110\}$ and $\{123\}$ were difficult to identify because they require significant structural relaxations (Table 4.3). These relaxations are illustrated in Fig. 4.12.

The similarity in ideal strengths on the three slip systems is due to two factors: the similarity in the instability strains and the isotropy of the shear modulus. As shown in Table 4.3, the primary strains at instability vary by only a few percent, from 0.168 for $\{112\}$ to 0.182 on $\{123\}$. In each case, the instability strain is about one-half of the primary strain to the first extremum,

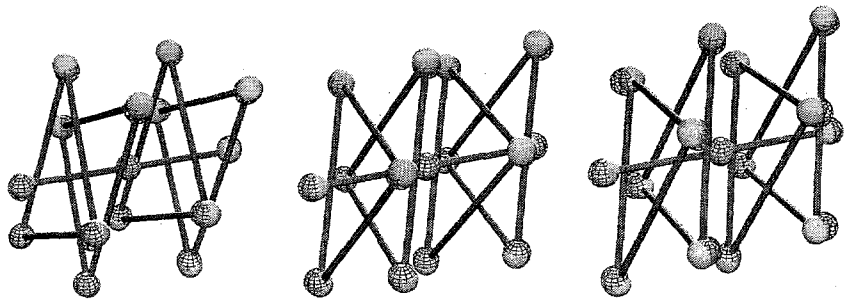

{110} {112} {123}

Figure 4.12: Illustrations of the relaxations from the applied simple shear strain to the saddle points for slip on {110}, {112}, and {123} planes. The cages represent the positions of the atoms after simple shear. The spheres represent the atoms after relaxation. The relaxed positions of {112} and {123} differ by only a rotation of approximately 10 degrees about ⟨111⟩.

which varies from ≈ 0.32 for {110} to ≈ 0.35 for {112}. If we approximate the stress-strain relation by a sine wave, as in Eq. (4.10), with a period of 0.34, and require that Hooke's Law be satisfied at small strains, the relaxed shear stress, τ, is approximately

$$\tau \approx \tau_m \sin\left[\frac{\pi\gamma}{0.34}\right], \tag{4.12}$$

giving the ideal strength as

$$\tau_m \approx \left[\frac{0.34}{\pi}\right] G = 0.11\, G. \tag{4.13}$$

This estimate agrees very well with the results of the *ab initio* calculations (Table 4.2).

Equation (4.13) suggests that the virtual identity of the ideal shear strengths on the three bcc slip systems in W is due in large part to its isotropic shear modulus. It further suggests that the ideal shear strengths in less isotropic bcc crystals will vary systematically with their shear moduli. In fact, this is not true. The modulus for shear will, in general, depend on both the shear direction and the shear plane, but, because of the threefold symmetry for rotation about ⟨111⟩ in bcc, any shear in a ⟨111⟩ direction has a relaxed modulus of

$$G^{\tau}_{\langle 111\rangle} = \frac{1}{s_{\langle 111\rangle}} = \frac{3\,c_{44}(c_{11}-c_{12})}{4\,c_{44}+c_{11}-c_{12}}. \tag{4.14}$$

This means that Eq. (4.13) can be used to predict the shear strength of any bcc metal and that the strength on any system $\langle 111\rangle\{ijk\}$, where $i+j=k$, will be nearly identical.

4.4 Comparison with Experiment

The experimental observations that may be clarified by these results include qualitative observations on the deformation and fracture of tungsten and similar bcc metals, and quantitative data on the ultimate strength of W, obtained from tensile tests on whisker crystals and nanoindentation tests on W films.

4.4.1 Brittle fracture

Like other bcc transition metals, polycrystalline tungsten fractures in a brittle mode at low temperature by cleavage on {100} planes. As discussed above, the {100} cleavage plane is dictated by symmetry. Since a relaxed stretch along ⟨110⟩ produces the fcc structure at moderate strain, the crystal is weak in tension in that direction. The weakness on ⟨100⟩ is confirmed by the *ab initio* calculations of Šob *et al.* [38], and their result for the ideal strength is confirmed in the present work.

There is at least some evidence that the simple estimate of the cleavage strength given in Eq. (4.11) is applicable to other bcc metals. We have completed a preliminary calculation of the cleavage strength of bcc Fe, and have found a value of 10.5 GPa, which is almost precisely $0.08\,E_{\langle 100\rangle}$.

Despite its tendency to cleave on {100}, whether an ideal single crystal of W fails by fracture or by shear depends on how it is loaded. If any of the common slip systems is loaded in simple shear to the elastic limit ($\approx$ 18 GPa), the maximum tensile strength on any plane is also about 18 GPa. Since this stress is well below the minimum tensile strength, 29 GPa in ⟨100⟩, an ideal crystal loaded in simple shear should fail in a shear instability that would (probably) resolve itself by plastic deformation through twinning or dislocation nucleation and glide. If, however, an ideal crystal were loaded in ⟨100⟩ tension to the cleavage stress, 29 GPa, the maximum resolved shear stress would only be 14.5 GPa, which is below the ideal shear strength. It follows that an ideal W crystal that is loaded in ⟨100⟩ tension at low temperature will cleave before plastic deformation intrudes.

4.4.2 "Pencil glide"

The most striking characteristic of the shear strength is its virtual degeneracy for ⟨111⟩ slip in the {110}, {112} and {123} planes. At least at moderate to high temperature, the deformation of a typical bcc crystal is characterized by slip on planes that include the ⟨111⟩ direction, among which these three are the most prominent [70, 71, 83]. The identity of the slip plane is sometimes so difficult to determine that the deformation is described as "pencil glide" in the ⟨111⟩ direction. The choice of slip plane is made by mobile dislocations and has no automatic association with the ideal strength. It may, therefore, be merely interesting that the ideal shear strength has a very similar crystallographic degeneracy. On the other hand, the lattice strain becomes large in the dislocation core, and that finite strain must be propagated as it moves, so the

Table 4.4: Experimental estimates of ideal shear strength: maximum normal stress ($\sigma_{\max}$), maximum shear stress ($\tau_{\max}$) and normalized shear stress ($\tau_{\max}/G$).

	failure stress		
	$\sigma_{\max}$ (GPa)	$\tau_{\max}$ (GPa)	$\tau_{\max}/G$ (%)
whiskers[a]	24.7 ± 3.6	12.5 ± 1.8	7.8 ± 1.1
nanoindentation[b]	69.6 ± 3.7	21.6 ± 1.1	13.5 ± 0.7

[a]Fracture of ⟨110⟩ whiskers [84].
[b]Nanoindentation of a ⟨100⟩ surface [85]. A single observation of $\tau_{\max}$ = 28.6 GPa was also noted.

considerations that lead to degeneracy in the strength also favor degeneracy in dislocation slip.

4.4.3 Experimental values of the ideal strength

Table 4.4 shows two of the most recently determined values of the ideal shear strength of W, one measured on nominally dislocation-free "whiskers" [84] and one measured via nanoindentation on lightly oxidized W films [85].

Whisker data

Mikhailovskii *et al.* [84] studied the tensile fracture of microcrystalline tungsten "whiskers" with diameters in the range 600–2600Å and long axes parallel to ⟨110⟩. The maximum strength was 28.3 GPa.

While we did not calculate strength for a tensile pull along ⟨110⟩, Šob *et al.* [38] found a value of approximately 54 GPa for tensile fracture. Given that the load is never precisely along a ⟨110⟩ axis, the crystal might instead be expected to fail at a load close to that which provides a resolved shear stress equal to the shear strength on the most favorably oriented plane. This criterion suggests failure when the tensile stress along ⟨110⟩ is about 36 GPa, or twice the ideal shear strength.

It follows that the maximum whisker strength is about 0.80 of the theoretical value. This is satisfying for two reasons. First, the computed ideal strengths should always be slightly greater than any experimental observations. Second, prior work [53] suggests a mechanism for this difference: the failure of whiskers ordinarily originates from free surfaces. This suggests that the strength of whiskers is determined by heterogeneous nucleation of defects at free surfaces rather than by the bulk value of the ideal strength.

Nanoindentation measurements

Nanoindentation tests probe the mechanical response to indentation by an indenter that is no more than a few nanometers in diameter [86–88]. If the material tested has a low dislocation density then the nanoindenter may probe essentially defect-free material. If, in addition, the surface of the crystal is treated to prevent premature failure from the interface, then failure may be made to originate in the region of maximum stress beneath the interface. It follows that nanoindentation studies are a promising method for measuring the bulk value of the ideal strength.

The most extensive study of the nanoindentation of tungsten was by Bahr *et al.* [85]. They inferred the shear stress at yielding by using the depth of indentation by the indenter in the familiar Hertz solution for the stress field of an elastic indenter. They report a maximum shear stress at yield of 28 GPa, and report a number of measurements at about 26 GPa. These values are significantly above our calculated value of the ideal shear strength (18 GPa).

Aside from experimental or theoretical errors, there are at least two possible sources for this discrepancy. The first is the triaxiality of the load at yield: the material is subject to a hydrostatic stress that is of the same order of magnitude as the shear stress. While this issue deserves a specific investigation, the work of Söderlind and Moriarty [42] on the behavior of Ta at high pressure suggests that pressure has no dramatic effect on the shear strength until pressures significantly larger than those encountered here.

A more immediate concern is the applicability of the Hertz solution for the elastic strain field, which assumes a linear elastic stress-strain response and elastic isotropy. Neither assumption is true when the strain approaches elastic instability. Figure 4.6 shows clearly the non-linear elastic behavior near instability. The assumption of elastic isotropy no longer holds because, while the effective shear modulus in the soft direction vanishes at the point of instability, the moduli for shear modes perpendicular to the soft direction remain large.

A rough estimate of the correction needed to account for the softening of the modulus near instability can be made as follows.[†] The displacement at the indenter-substrate interface, which is used to compute the Hertzian strain field, is set by the net modulus of the whole substrate volume strained by the indenter. Since almost all of this volume responds in a linear elastic mode, the strain field computed from the indentation should not be all that wrong, even if the small volume of material that is under a high shear stress responds in a non-linear way. Assuming that the estimated shear strain at failure is approximately correct, and further assuming a sinusoidal stress-strain relation, we have

$$\tau = \tau_m \sin\left[\frac{\pi\gamma}{2\gamma_m}\right], \tag{4.15}$$

where γ_m is the strain at failure and τ_m is the strength. Since $\tau = G\gamma$ for small

[†]The derivation of this $\pi/2$ correction is the work of D. Roundy.

strains,

$$\tau_m = \frac{2}{\pi} G\gamma_m = \frac{2}{\pi}\tau_m^0, \tag{4.16}$$

where τ_m^0 is the strength computed from the same failure strain on the assumption of linear elasticity.

Equation (4.16) suggests that the strengths back-calculated from the Hertzian strain field should be multiplied by a factor of about $2/\pi$ for comparison to the ideal strength. This factor corrects the W measurements of Bahr *et al.* [85] from 26–28 GPa to 16.5–18 GPa, in very good agreement with the theoretical numbers. The agreement is very likely to be better than the accuracy of this simple model, but it does support the notion that nanoindentation experiments do measure the ideal strength in shear.

4.5 Conclusion

We have used pseudopotential density functional theory within the local density approximation to calculate the ideal tensile strength of tungsten pulled in a $\langle 100\rangle$ direction and the ideal shear strengths for the $\langle 111\rangle\{110\}$, $\langle 111\rangle\{112\}$ and $\langle 111\rangle\{123\}$ slip systems, allowing full structural relaxation of the strains orthogonal to the applied shear. We also computed the shear strength in the $\langle 110\rangle\{110\}$ system for comparison.

The ideal tensile $\langle 100\rangle$ tensile strength was found to be 29.5 GPa. This number ($= 0.072\,E_{\langle 100\rangle}$) is in close agreement with prior calculations. This number is also in good agreement with the value ($0.08\,E_{\langle 100\rangle}$) expected for a material that has a sinusoidal stress-strain relation and a tensile strength that is determined by the "Bain" instability on $\langle 100\rangle$. The shear strength was close to 18 GPa ($0.11\,G$) for all three slip systems. Analysis of the structural relaxations that occur during these shears revealed that the ideal shear strengths are determined by relatively high-symmetry extrema that are reached in each of these systems after a shear of 0.32–0.35. These extrema are related to the packing sequence along $\langle 111\rangle$ directions in the bcc lattice. The shear strengths are also in good agreement with a model that uses a sinusoidal approximation for the stress-strain relation. Finally, as expected, the strength in the $\langle 110\rangle\{110\}$ system is higher than that in any of the three $\langle 111\rangle$-based systems commonly observed in bcc.

The calculated shear strengths are, at least, in the range of the values obtained from tensile tests on tungsten "whiskers" and nanoindentation tests of tungsten films. The maximum tensile strengths of whiskers are about 0.8 of the expected values. We suspect this reflects early failure of these thin whiskers from surface-induced defects. The maximum shear strengths reported from nanoindentation experiments are almost 1.5 times the theoretical value. We believe this discrepancy is primarily due to the linear elastic assumption used to extract the strength from the experimental data. If we use a sinusoidal stress-strain relation

to correct the stress at given strain, the reported measurements are corrected by a factor of $2/\pi$, which reduces them to the theoretical numbers.

Chapter 5

Summary and Future Work

5.1 Summary

This dissertation has critically examined a number of scaling relationships between atomic-scale properties and intrinsic mechanical hardness. For the majority of materials examined, hardness scales linearly with elastic shear modulus for a given bonding type (covalent, ionic or metallic). However, we have identified a technologically important class of materials where this scaling relationship does not hold: the group IVa and Va transition metal carbides and nitrides. As a class, the group IVa and Va transition metal carbides have higher mechanical hardnesses for a given shear modulus than the corresponding nitrides despite having the identical crystal structure and very similar bonding.

In an attempt to understand why and how the scaling of hardness with shear modulus can break down, we have developed a detailed theoretical analysis of "ideal strength," which is defined by the limit of elastic stability of a quasi-statically loaded perfect crystal. In general, the conditions of stability are contained in the requirement that $\lambda_{ijkl}\delta\epsilon_{ij}\delta\epsilon_{kl} \geq 0$ for all infinitesimal strains, where $\lambda_{ijkl} = \frac{1}{2}(B_{ijkl} + B_{klij})$, and $\boldsymbol{B}$ is the tensor that governs the change in the Cauchy stress ($\boldsymbol{t}$) during incremental strain from a stressed state (τ) : $t_{ij} = \tau_{ij} + B_{ijkl}\delta\epsilon_{kl}$. Stability is lost when the minimum eigenvalue of λ_{mn} (the 6×6 Voigt form) vanishes.

Ideally, one would hope to use *ab initio* computations to determine $\boldsymbol{B}$ as a function of applied strain, but this is computationally very expensive. In Chapter 3, we justify a much more computationally efficient approach that calculates only energy and stress as a function of strain. The ideal strength for any uniaxial loading direction (including shear) can be determined by allowing full atomic relaxation perpendicular to the applied strain. This maps out a minimum energy path for the deformation, and the ideal strength is determined by locating the maximum of stress along the path. If the axis of applied strain is along a high symmetry direction, this procedure may miss instabilities along directions perpendicular to the direction of stretch, but these instabilities can

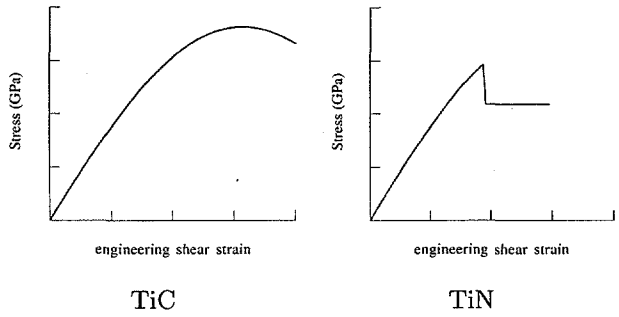

Figure 5.1: Schematic illustration of the stress–strain behavior for $\langle 1\bar{1}0\rangle\{110\}$ shear in TiC and TiN

be detected by combining the uniaxial procedure with a few low symmetry distortions and a bit of physical insight.

Chapters 2 and 4 present *ab initio* ideal strength calculations using these techniques for Al, Cu and W. These are the first *ab initio* calculations that incorporated full atomic relaxation perpendicular to the applied strain, and they show that relaxation can have very important effects. For Al and Cu, relaxation reduces the values of ideal shear strength by 35% to 45%, resulting in strengths of 8–9 percent of the shear modulus for both Al and Cu. For W, relaxation produced the remarkable result that the ideal strengths on {110}, {112}, and {123} planes were nearly identical (≈ 18 GPa $= 0.11\,G$). Encouragingly, with a small correction that accounts for the non-linear stress–strain behavior near instability, this strength is very close to the shear strengths determined from nano-indentation experiments. The equivalence of the strengths on all three common bcc slip planes is explained in terms of bcc's linear elastic isotropy for shears in a $\langle 111\rangle$ direction and of the atomic configurations of the energetic saddle points reached during shear. Chapter 4 also analyzes the *ab initio* results in terms of a simple Frenkel-Orowan crystallographic model.

5.2 Preliminary Results in TiC and TiN

This dissertation began with the problem of identifying why TiC had a microhardness 50% higher than TiN despite having essentially the same value of the elastic shear modulus. Preliminary *ab initio* calculations of the ideal strength of TiC and TiN suggest an explanation [89]. Figure 5.1 schematically shows the stress–strain behavior for $\langle 1\bar{1}0\rangle\{110\}$ shear in both TiC and TiN. While the stress–curve for TiC is roughly sinusoidal, there is a discontinuity in the curve for TiN. This discontinuity corresponds to an internal structural instability in TiN. Figure 5.2a shows the AB stacking sequence along the $\langle 001\rangle$ direction in TiC and TiN at small strains. Each C or N atom is surrounded by six neigh-

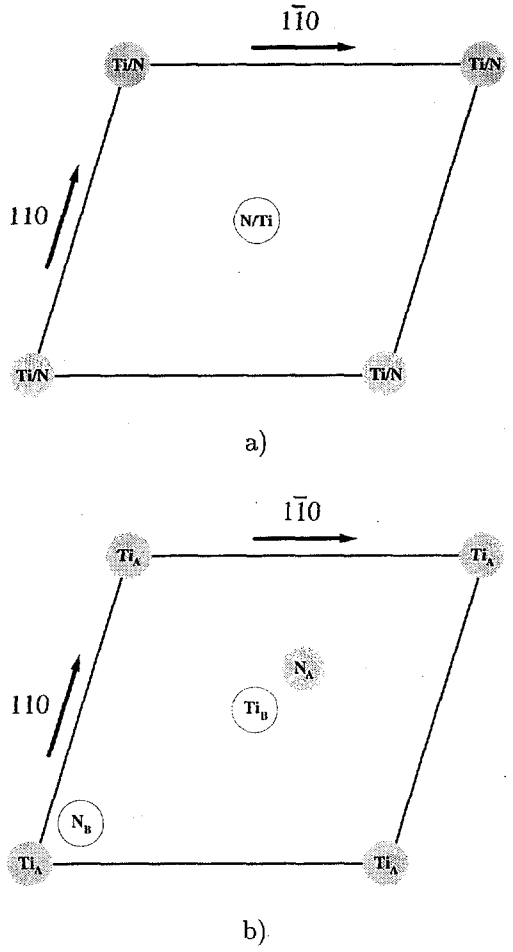

Figure 5.2: Illustration of instability in TiN during $\langle 1\bar{1}0\rangle\{110\}$ shear: a) Stacking sequence ($ABAB$) along $\langle 001\rangle$ for both TiC and TiN after a small amount of $\langle 1\bar{1}0\rangle\{110\}$ shear. b) Stacking sequence (also $ABAB$) in TiN after elastic instability.

boring Ti atoms: four in the $\{001\}$ plane and two above and below the central atom. At large strains in TiN however, the nitrogen spontaneously shifts from the central six-fold coordinated octahedral void to a five-fold coordinated void illustrated in Fig. 5.2b. Because this shift does not occur in TiC, TiC has a significantly higher ideal strength than TiN. This may be an explanation why TiC also has a significantly higher measured microhardness as well.

5.3 Future Work

5.3.1 Computations

This dissertation presented *ab initio* calculations of the ideal shear strength of Al and Cu, the ideal shear and tensile strengths of W, and qualitative results of the ideal shear strengths of TiC and TiN. Computations of the ideal strengths of Mo, Fe, Si and diamond are currently underway [90]. Calculations in a pair of hcp metals and a number of representative ionic materials would also be of great interest.

The *ab initio* calculations relate, strictly, to perfect crystals in the limit of zero temperature. These calculations also were quasistatic and uniaxial. In order to estimate the effect of phonons at finite temperature and the effect of multiaxial loading, which may be important for comparison with nano-indentation experiments, we have begun a series of embedded-atom method (EAM) calculations. EAM is much less computationally intensive than *ab initio* techniques, but it can offer an estimate of the magnitude of the phonon and multiaxial loading effects. These ongoing EAM studies [74] can also identify situations in which further analysis with *ab initio* techniques is warranted.

5.3.2 The relaxation strain

The atomic relaxations at large strain in Al and Cu are consistent with experimental observations of third-order elastic constants. It will be of interest to analyze the third-order elastic constants measured for Fe, Mo, Na and Nb [10] to determine whether these detect the "pencil glide" saddle point found in our calculations. It also may be possible to confirm the relaxations predicted by our calculations with high resolution transmission electron microscopy (TEM) around dislocation cores or near highly strained coherent phase boundaries. Because the lattice instability in TiN occurs at a large applied strain, it is unlikely to affect measured higher order elastic constants, but TEM observations or phonon spectra of highly strained thin films might detect the instability.

5.3.3 Brittle fracture

We argued in Section 4.4.1 that the brittleness of bcc metals can be understood by the relatively small bain strain (= 0.26) required to produce fcc by tensile deformation of bcc along ⟨100⟩. Unfortunately, the same argument seems to suggest that the ⟨110⟩ tensile strength of fcc would be even smaller than the ⟨100⟩ strength of bcc. A constant volume bain strain of only 0.12 along ⟨110⟩ will transform fcc into bcc. From this, Eq. 4.11 predicts an ideal tensile strength of only $0.04\,E_{\langle 110\rangle}$ and suggests that fcc would be more brittle than bcc.

However, this prediction presumes that the stress–strain curve is sinusoidal and that the minimum energy deformation path for ⟨110⟩ uniaxial tension in fcc is the bain transformation path. Neither presumption is necessarily true. Because of the symmetry of the transformation, a much larger orthogonal re-

laxation ($= 0.21 = 1 - 1/1.26$) is necessary to transform from fcc to bcc. Instead of using a uniaxial sinusoidal fit to energy, it may be more appropriate to analyze the total stored elastic energy along the deformation path. Symmetry suggests that the elastic work required to reach the saddle point between fcc and bcc will be comparable whether one starts at fcc or bcc. Energy balance also requires that the work done by the applied stress be equal to the internal elastic strain energy. Since for the transformation from fcc to bcc this stress is applied over half the distance needed for the bcc to fcc transformation, the maximum stress required for the fcc to bcc transformation will be approximately twice as large as the bcc to fcc case. This suggests that a sinusoidal fit will not work for $\langle 110 \rangle$ loading in fcc but that the normalized ideal strengths for this loading will be twice the normalized ideal strengths for $\langle 100 \rangle$ tension in bcc.

Although calculations of ideal strength for $\langle 110 \rangle$ tension using empirical EAM potentials found fcc metals to be weak along $\langle 110 \rangle$ [72], the *ab initio* calculations of Šob *et al.* [91] call into question the presumption that $\langle 110 \rangle$ loading will follow the bain transformation path. They have calculated the strength of Cu for relaxed loading along $\langle 110 \rangle$ and found a peak stress of 31 GPa at a strain of 0.79. This result ($\approx 0.24\, E_{\text{avg}}$) suggests that the minimum energy deformation path did not pass anywhere near the metastable bcc Cu phase.

It would be of interest to analyze the *ab initio* stress–strain behavior of Cu constrained along the bain deformation path. It would also be useful to analyze the atomic relaxations along the minimum energy $\langle 110 \rangle$ path.

5.3.4 "Pencil glide"

Understanding the atomic relaxations during shear in bcc also could offer a much better understanding of the prevalence of the pencil glide of dislocations on planes containing a $\langle 111 \rangle$ direction in bcc metals. Section 4.3.4 showed that the minimum ideal strength in shear on any slip plane containing $\langle 111 \rangle$ will be nearly constant. However, some experimental observations, particularly careful measurement and modeling of crystallographic texture evolution during plastic deformation of bcc metals [92] suggest that the critical resolved stresses for slip differ for different "pencil glide" systems. It would be of great interest to explore whether this can be explained by combining our new knowledge of the crystallography of pencil glide with anisotropic elasticity theory of dislocations or whether detailed calculations of dislocation core structures are necessary to understand these experimental observations.

5.3.5 Dislocation or lattice control of strength

In Chapter 1, our working assumption was that dislocation motion governed the hardness of all materials. This assumption was made on the basis of a number of observations. 1) Since room temperature indentation hardness tests of even diamond leave permanent plastic deformation, it is clear that atomic shear has to occur. 2) In most materials (excepting Si [93, 94]) no evidence of

twinning or phase transformation is observed. 3) At high enough temperature, dislocations have observed to multiply and propagate during bulk deformation of all crystalline materials that have been examined. 4) Optical micrographs of the regions around hardness indentations reveal slip bands consistent with the crystallography of experimentally observed high temperature dislocations. 5) Many electron (TEM) micrographs of the regions around indentations reveal dislocations that seem to have initiated at the indentation and propagated a small distance away.

If the Peierls stress is small relative to the stresses required for other mechanisms of deformation, the circumstantial observations in the previous paragraph are sufficient to convince all but the most skeptical that dislocation motion is the mechanism of deformation. By comparing the normalized Peierls stress τ_p/G to the normalized ideal shear strength $\tau_{\max}/G$, we see that this is clearly the case for metals. Table 1.3 shows that our best estimate of τ_p/G is 0.01 or less for most metals and our calculations in Al, Cu and W give $\tau_{\max}/G$ as 0.08–0.11. However, for hard materials (Table 1.1), τ_p/G can be 0.1 or larger. Preliminary calculations of the ideal shear strengths of diamond and silicon show that $\tau_{\max}/G$ is 0.2–0.3 [90].

When $\tau_{\max}$ is of the same order of magnitude as τ_p, homogeneous dislocation nucleation becomes almost as easy as dislocation propagation. However, a simple energetic argument suggests that the minimum stress needed to move an isolated dislocation or dislocation kink will always be less than the stress needed to nucleate a dislocation of the same slip system in a perfect crystal, and that $\tau_{\max}$ sets an upper bound for τ_p: The presence of a dislocation should not affect the period of the instability, but it should increase the ground state energy more than the saddle point energy. If this is true (Fig. 5.3), then the instability stress (the maximum slope of the energy–strain curve) will be lowered by the presence of the dislocation. For this argument to hold in general requires that the minimum strength in shear to occur on the same slip system as the slip system for easy dislocation glide. This is the case for fcc and bcc metals and appears to be the case for the NaCl and diamond cubic structures as well.[†]

Even though τ_p is theoretically always smaller than $\tau_{\max}$, if τ_p is a large fraction of $\tau_{\max}$, there can be many situations in which it may be easier to homogeneously nucleate new dislocations than it is to move and multiply existing dislocations. The only way to definitely determine the mechanism of deformation in hard materials is to perform *in situ* nano-indentation experiments in a TEM to directly observe the relative importance of homogeneous dislocation nucleation and dislocation propagation. These experiments (using TiC) are ongoing at the National Center for Microscopy (NCEM) at Lawrence Berkeley National Lab [95].

[†]Note: There is one additional complication to this argument. Even if the instability stress is lowered, it has not yet been proven that the existing dislocation will move when this stress is reached. The dislocation may instead catalyze another deformation mode in the crystal.

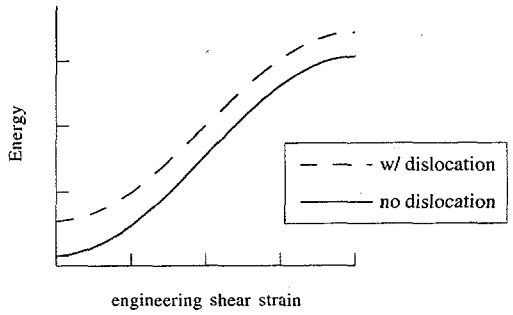

Figure 5.3: Schematic illustration of the effect of a dislocation on the energy–strain curve.

Appendix A

Scaling of Elastic Moduli

A.1 Scaling with Lattice Constant

Chapter 1 showed that hardness scales very closely with elastic moduli for a given class of material but that covalent materials have the highest hardnesses for a selected value of the elastic shear or bulk moduli. Given these observations, the simplest way to find a material harder than diamond is to look for a covalent material with a higher shear or bulk modulus than diamond. One way to begin this search is to use a scaling relationship between bulk modulus and lattice constant.

Cohen [96] developed such a relationship by starting with a previous derivation of the bulk modulus of a free-electron gas. For a free electron gas, the bulk modulus K is given as

$$K = \frac{2}{3} n E_F = \left(\frac{6.13}{r_s}\right)^3 \text{GPa}, \tag{A.1}$$

where E_F is the Fermi energy, n is the electron concentration, and r_s is the electron gas parameter. For covalent materials, however, Cohen determined the relevant energy scale to be the homopolar gap E_h and the relevant volume to be the volume of the covalent bond. Combining experimental observations and *ab initio* computations of covalent bond geometries and a previously observed scaling relation for E_h yields an expression for the bulk modulus of covalent materials as follows:

$$K = 1761\, b^{-3.5}, \tag{A.2}$$

where b is the nearest-neighbor distance. This expression predicts the bulk moduli of diamond, Si and Ge to within 2% of the experimental values. It also predicts bulk moduli within 3% (except for InP) for III-V semiconductors but is less successful for II-VI semiconductors, which have a significantly higher degree of ionicity in their bonding. The empirical result [96],

$$K = (1971 - 220\lambda) b^{-3.5}, \tag{A.3}$$

more accurately describes the bulk moduli of the group IV ($\lambda = 0$), group III-V ($\lambda = 1$), and group II-VI ($\lambda = 2$) semiconductors. Cohen [96] cites the scaling behavior of the I-VII alkali halides as having a scaling exponent of -3:

$$K = 550\, b^{-3}. \tag{A.4}$$

Using Eq. (A.2) and tabulated values of ionic and covalent radii, Cohen predicted that a tetravalent compound of C and N would have a bulk modulus of between 461 and 483 GPa. This modulus would be significantly higher than diamond. However, because of the lone pair of electrons on N, it is geometrically impossible to construct a completely tetravalent lattice from C and N. The most densely packed and stable IV-V structure known, Si_3N_4, has only 6 covalent bonds for every 7 bonds that would be possible in a fully tetravalent structure. First-principles calculations [2] show that the bulk modulus of C_3N_4 (427 ± 15 GPa) seems to be slightly smaller than diamond (442 ± 0.7 GPa).

For reference purposes, I have included plots of bulk modulus as a function of nearest-neighbor distance (Figs. A.1–A.3). The data is tabulated in Tables 1.1–1.3. Power law curve fits to this data yield the following expressions:

covalent materials	$K = 2226 \times b^{-3.76}$	$R = 0.9992$	(A.5)
ionic oxides	$K = 1734 \times b^{-3.13}$	$R = 0.996$	(A.6)
ionic alkali halides	$K = 594 \times b^{-3.06}$	$R = 0.95$	(A.7)

These three empirical fits are very close to the expressions theoretically derived by Cohen. For the metals in Fig. A.3, bulk modulus scales roughly as b^{-6}, but there is a great deal more scatter.

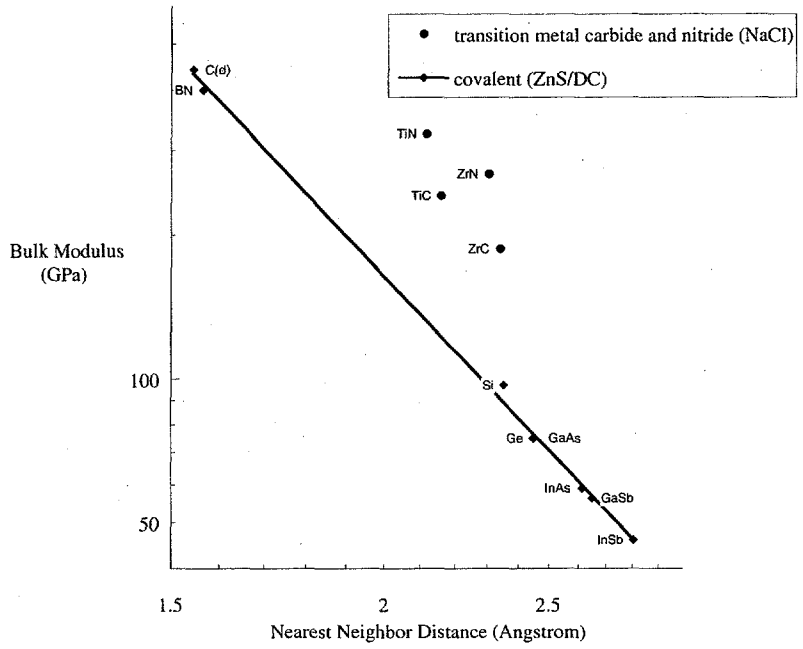

Figure A.1: Log-log plot of bulk modulus as a function of nearest-neighbor distance for covalent materials with the diamond cubic (dc), NaCl, and ZnS structures.

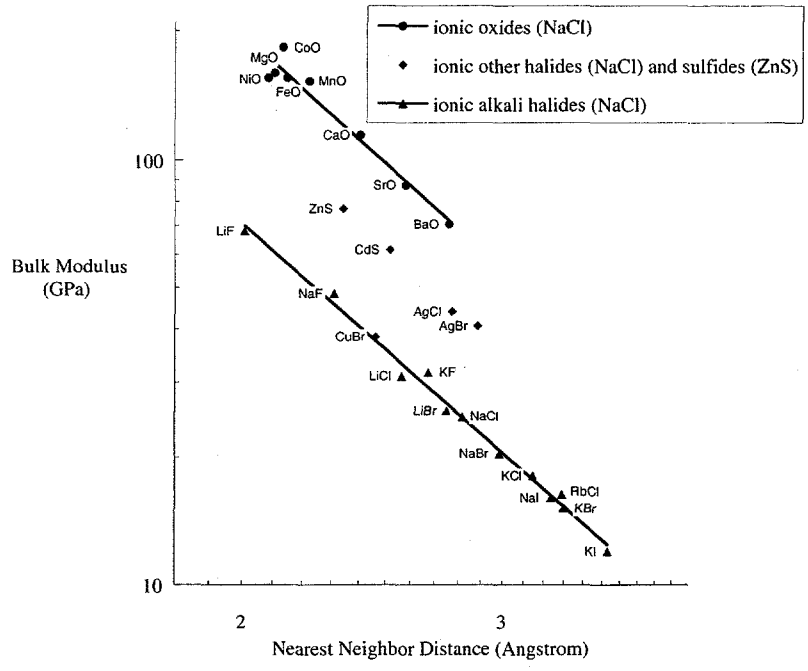

Figure A.2: Log-log plot of bulk modulus as a function of nearest-neighbor distance for ionic materials with the NaCl and ZnS structures.

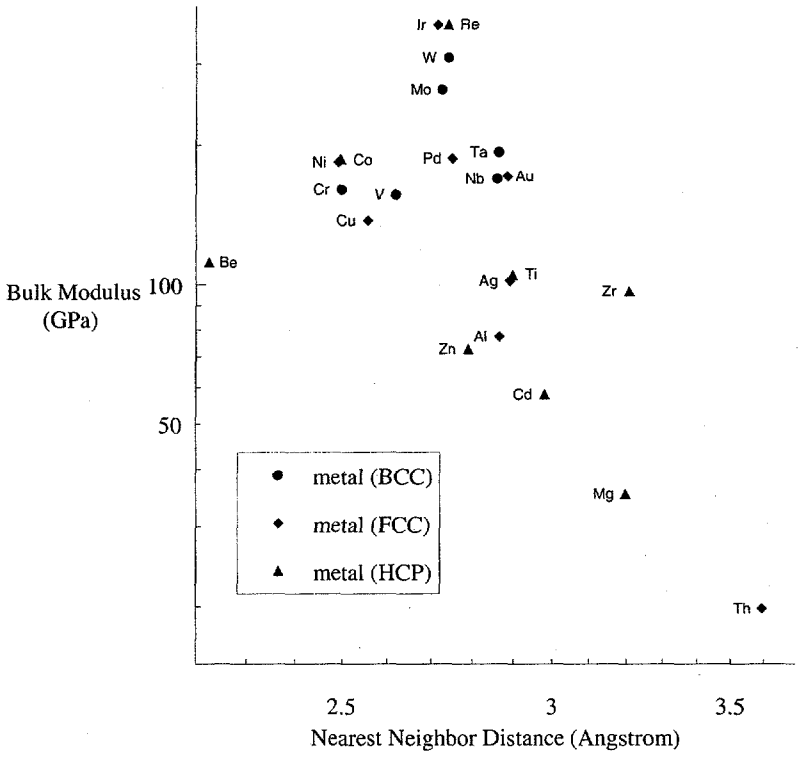

Figure A.3: Log-log plot of bulk modulus as a function of nearest-neighbor distance for metallic materials with the body-centered cubic (bcc), face-centered cubic (fcc), and hexagonal close-packed (hcp) structures.

Bibliography

1. C. R. Krenn, J. W. Morris, Jr., S.-H. Jhi and J. Ihm, in *Hard Coatings Based on Borides, Carbides & Nitrides* (edited by A. Kumar, Y.-W. Chung and R. W. J. Chia), pp. 379–388, TMS (1998).

2. A. Y. Liu and M. L. Cohen, *Science* **245**, 841 (1989).

3. D. M. Teter and R. J. Hemley, *Science* **271**, 53 (1996).

4. J. N. Plendl and P. J. Gielisse, *Phys. Rev.* **125**, 828 (1962).

5. R. J. Goble and S. D. Scott, *Can. Mineral.* **23**, 273 (1985).

6. J. J. Gilman, *Aust. J. Phys.* **13**, 327 (1960).

7. D. M. Teter, *MRS Bull.* **23**, 22 (1998).

8. J. J. Gilman, *Mater. Sci. Eng. A* **209**, 74 (1996).

9. J. E. Field, *The Properties of Natural and Synthetic Diamond*, Academic Press, London (1992).

10. D. F. Nelson (ed.), *Landolt-Börnstein LBIII/29a—Low Frequency Properties of Dielectric Crystals: Second and Higher Order Elastic Constants*, Springer-Verlag, Berlin (1992).

11. R. W. G. Wyckoff, *Crystal Structures*, Interscience Publishers, New York, 2nd ed. (1963).

12. A. A. Ivan'ko, *Handbook of Hardness Data*, Israel Program for Scientific Translations, Jerusalem (1971).

13. H. Holleck, *J. Vac. Sci. Technol. A* **4**, 2661 (1986).

14. M. M. Yang, J. L. Chao and M. A. Russak, *IEEE Trans. Magn.* **33**, 3145 (1997).

15. N. Alexandre, M. Desmaison-Brut, F. Valin and M. Boncoeur, *J. Mater. Sci.* **28**, 2385 (1993).

16. J. O. Kim, J. D. Achenback, M. Shinn and S. A. Barnett, *J. Mater. Res.* **7**, 2248 (1992).

17. R. Ahuja, O. Eriksson, J. M. Wills and B. Johansson, *Phys. Rev. B* **53**, 3072 (1996).

18. M. Grimsditch, E. S. Zouboulis and A. Polian, *J. Appl. Phys.* **76**, 832 (1994).

19. E. Knittle, R. M. Wentzcovitch, R. Jeanloz and M. L. Cohen, *Nature* **337**, 349 (1989).

20. G. Beckmann, *Kristall und Technik* **6**, 109 (1971).

21. G. Simmons and H. Wang, *Single Crystal Elastic Constants and Calculated Aggregate Properties: A Handbook*, M. I. T. Press, Cambridge, Mass. 2nd ed. (1971).

22. Z. Hashin and S. Shtrikman, *J. Mech. and Phys. Solids* **10**, 335 (1962).

23. Z. Hashin and S. Shtrikman, *J. Mech. and Phys. Solids* **10**, 343 (1962).

24. R. E. Peierls, *Proc. Phys. Soc. Lond.* **52**, 34 (1940).

25. F. R. N. Nabarro, *Proc. Phys. Soc. Lond.* **59**, 256 (1947).

26. F. R. N. Nabarro, *Phil. Mag. A* **75**, 703 (1997).

27. H. B. Huntington, *Proc. Phys. Soc. B* **68**, 1043 (1955).

28. K. Ohsawa, H. Koizumi, H. O. K. Kirchner and T. Suzuki, *Phil. Mag. A* **69**, 171 (1994).

29. A. J. Foreman, M. A. Jaswon and J. K. Wood, *Proc. Phys. Soc. A* **64**, 156 (1951).

30. R. Bullough, A. B. Movchan and J. R. Willis, in *Materials Modelling: from Theory to Technology* (edited by C. A. English, J. R. Matthews, H. Rauh, A. M. Stoneham and R. Thetford), pp. 73–78, IOP Publishing, London (1992).

31. D. Roundy, C. R. Krenn, M. L. Cohen and J. W. Morris, Jr., *Phys. Rev. Lett.* **82**, 2713 (1999).

32. C. R. Krenn, D. Roundy, J. W. Morris, Jr. and M. L. Cohen, *Mater. Sci. Eng. A* (1999), in press.

33. D. Roundy, C. R. Krenn, M. L. Cohen and J. W. Morris, Jr., *LBNL Report No. 44373* (1999), submitted for publication.

34. A. Kelly and N. H. Macmillan, *Strong Solids*, Clarendon Press, Oxford, 3rd ed. (1986).

35. J. W. Morris, Jr., C. R. Krenn, D. Roundy and M. L. Cohen, in *Proceedings of the Hume-Rothery Symposium* (edited by P. E. A. Turchi and A. Gonis), TMS, Nashville (2000), in press.

36. M. L. Cohen, *Phys. Scr.* **T1**, 5 (1982).

37. M. Šob, L. G. Wang and V. Vitek, *Mat. Sci. Eng. A* **234–236**, 1075 (1997).

38. M. Šob, L. G. Wang and V. Vitek, *Phil. Mag. B* **78**, 656 (1998).

39. W. Li and T. Wang, *J. Phys.: Condens. Matter.* **10**, 9889 (1998).

40. A. T. Paxton, P. Gumbsch and M. Methfessel, *Phil. Mag. Lett.* **63**, 267 (1991).

41. W. Xu and J. A. Moriarty, *Phys. Rev. B* **54**, 6941 (1996).

42. P. Söderlind and J. A. Moriarty, *Phys. Rev. B* **57**, 10340 (1998).

43. J. Ihm, A. Zunger and M. L. Cohen, *J. Phys. C* **12**, 4409 (1979).

44. D. M. Ceperley and B. J. Alder, *Phys. Rev. Lett.* **45**, 566 (1980).

45. J. P. Perdew and A. Zunger, *Phys. Rev. B* **23**, 5048 (1981).

46. B. G. Pfrommer, M. Côté, S. G. Louie and M. L. Cohen, *J. Comput. Phys.* **131**, 233 (1997).

47. N. Troullier and J. L. Martins, *Phys. Rev. B* **43**, 1993 (1991).

48. D. R. Hamann, M. Schlüter and C. Chiang, *Phys. Rev. Lett.* **43**, 1495 (1979).

49. A. E. Green and J. E. Adkins, *Large Elastic Deformations*, Clarendon Press, Oxford, 2nd ed. (1970).

50. A. van d Walle and G. Ceder, *Phys. Rev. B* **59**, 14992 (1999).

51. M. M. Dacorogna, M. L. Cohen and P. K. Lam, *Phys. Rev. B* **34**, 4865 (1986).

52. Y. Sun and E. Kaxiras, *Phil. Mag. A* **75**, 1117 (1997).

53. S. S. Brenner, *J. App. Phys.* **27**, 1484 (1956).

54. J. W. Morris, Jr. and C. R. Krenn, *Phil. Mag. A* (2000), in press.

55. M. Born, *Proc. Camb. Phil. Soc.* **36**, 160 (1940).

56. R. Hill, *Math. Proc. Camb. Phil. Soc.* **77**, 225 (1975).

57. R. Hill and F. Milstein, *Phys. Rev. B* **15**, 3087 (1977).

58. J. Wang, S. Yip, S. R. Phillpot and D. Wolf, *Phys. Rev. Lett.* **71**, 4182 (1993).

59. J. Wang, J. Li, S. Yip, S. R. Phillpot and D. Wolf, *Phys. Rev. B* **52**, 12627 (1995).

60. J. W. Gibbs, *Trans. Conn. Acad.* **3**, 108 (1876), (in *The Scientific Papers of J. Willard Gibbs, Vol. 1: Thermodynamics*, Ox Bow Press, Woodbridge, CT, (1993), pp. 55–353).

61. A. C. Eringen, *Mechanics of Continua*, Rober E. Krieger, Melbourne, Florida, 2nd ed. (1989).

62. A. E. Green and W. Zerna, *Theoretical Elasticity*, Clarendon Press, Oxford, 2nd ed. (1968).

63. C. Lanczos, *The Variational Principles of Mechanics*, Univ. Toronto Press, Toronto, Canada, 4th ed. (1970), pp. 80–86, 369–79.

64. D. C. Wallace, *Thermodynamics of Crystals*, John Wiley, New York (1972), pp. 14–32.

65. J. Wang, S. Yip, D. Wolf and S. R. Phillpot, *Physica A* **240**, 396 (1997).

66. L. D. Landau and E. M. Lifshitz, *Statistical Physics: Part 1*, Pergamon Press, Oxford, 3rd ed. (1980), pp. 65–68.

67. F. Milstein, R. Hill and K. Huang, *Phys. Rev. B* **21**, 4282 (1980).

68. F. Milstein and S. Chantasiriwan, *Phys. Rev. B* **58**, 6006 (1998).

69. P. Söderlind, J. A. Moriarty and J. M. Wills, *Phys. Rev. B* **53**, 14063 (1996).

70. J. W. Christian, *Metall. Trans. A* **14**, 1237 (1983).

71. P. Gilormini, B. Bacroix and J. J. Jonas, *Acta Metall.* **36**, 231 (1988).

72. F. Milstein and S. Chantasiriwan, *Phys. Rev. B* **58**, 6006 (1998).

73. J. W. Morris, Jr., Z. Guo and C. R. Krenn, in *Proceedings of the 19^{th} ASM Heat Treating Society Conference*, ASM, Cincinnati (1999), in press.

74. C. R. Krenn, D. C. Chrzan and J. W. Morris, Jr. (1999), Dept. Mat. Sci. Eng., Univ. California, Berkeley, unpublished research.

75. O. H. Nielsen and R. M. Martin, *Phys. Rev. B* **32**, 3780 (1985).

76. O. H. Nielsen and R. M. Martin, *Phys. Rev. B* **35**, 9308 (1987).

77. F. H. Featherston and J. R. Neighbours, *Phys. Rev.* **130**, 1324 (1963).

78. P. Söderlind, L. H. Yang, J. A. Moriarty and J. M. Wills, *Phys. Rev. B* **61**, 2579 (2000).

79. F. Milstein and J. Marschall, *Phil. Mag. A* **58**, 365 (1988).

80. J. Frenkel, *Z. Phys.* **37**, 572 (1926).

81. E. Orowan, *Rept. Prog. Phys.* **12**, 185 (1949).

82. T. I. Novichikhina, M. A. Baranov, M. D. Starostenkov and V. V. Romanenko, *Tech. Phys. Lett.* **22**, 218 (1996).

83. J. P. Hirth and J. Lothe, *Theory of Dislocations*, J. Wiley, New York, 2nd ed. (1982).

84. I. M. Mikhaĭlovskiĭ, P. Y. Poltinin and L. I. Fedorova, *Sov. Phys. Solid State* **23**, 757 (1981).

85. D. F. Bahr, D. E. Kramer and W. W. Gerberich, *Acta Mater.* **46**, 3605 (1998).

86. M. F. Doerner and W. D. Nix, *J. Mater. Res.* **1**, 601 (1986).

87. J. B. Pethica and W. C. Oliver, *Phys. Scr.* **T19**, 61 (1987).

88. W. C. Oliver and G. M. Pharr, *J. Mater. Res.* **7**, 1564 (1992).

89. S.-H. Jhi, D. Roundy, M. L. Cohen and S. G. Louie (2000), Dept. Phys., Univ. California, Berkeley, unpublished research.

90. D. Roundy and M. L. Cohen (1999), Dept. Phys., Univ. California, Berkeley, unpublished research.

91. M. Šob, L. G. Wang and V. Vitek, *Kovové Materiály* **36**, 145 (1998).

92. P. J. Maudlin, J. F. Bingert and R. K. Garrett, Jr., in *Multiscale Phenomena in Materials—Experiments and Modeling*, MRS (2000), in press.

93. I. V. Gridneva, Y. V. Milman and V. I. Trefilov, *Phys. Status Solidi A* **14**, 177 (1972).

94. A. Kailer, Y. G. Gogotsi and K. G. Nickel, *J. App. Phys.* **81**, 3057 (1997).

95. A. M. Minor, E. A. Stach and J. W. Morris, Jr. (2000), Lawrence Berkeley National Lab, Berkeley, CA, unpublished research.

96. M. L. Cohen, *Phys. Rev. B* **32**, 7988 (1985).

Colophon

This thesis was typeset with LaTeX using a modified version of ua-thesis.sty from the University of Arizona. Electronic structure computations were done with the U. C. Berkeley Cohen/Louie Group electronic structure code Paratec [46]. Analysis of Paratec's output was performed with Perl 5, Mathematica 3, and Microsoft Excel 98. Plots and visualization were done with KaleidaGraph 3, POVRay 3, and MiniCAD 7.